

Consistent kinetic modeling of compressible flows with variable Prandtl numbers: Double-distribution quasi-equilibrium approach

R. M. Strässle,^{*} S. A. Hosseini,[†] and I. V. Karlin[‡]

Computational Kinetics Group, Department of Mechanical and Process Engineering, ETH Zürich, 8092 Zürich, Switzerland[§]

(Dated: January 21, 2026)

A consistent kinetic modeling and discretization strategy for compressible flows across all Prandtl numbers and specific heat ratios is developed using the quasi-equilibrium approach within two of the most widely used double-distribution frameworks. The methodology ensures accurate recovery of the Navier–Stokes–Fourier equations, including all macroscopic moments and dissipation rates, through detailed hydrodynamic limit analysis and careful construction of equilibrium and quasi-equilibrium attractors. Discretization is performed using high-order velocity lattices with a static reference frame in a discrete velocity Boltzmann context to isolate key modeling aspects such as the necessary requirements on expansion and quadrature orders. The proposed models demonstrate high accuracy, numerical stability and Galilean invariance across a wide range of Mach numbers and temperature ratios. Separate tests for strict conservation and measurements of all dissipation rates confirm these insights for all Prandtl numbers and specific heat ratios. Simulations of a thermal Couette flow and a sensitive two-dimensional shock-vortex interaction excellently reproduce viscous Navier–Stokes–Fourier-level physics. The proposed models establish an accurate, efficient and scalable framework for kinetic simulations of compressible flows with moderate supersonic speeds and discontinuities at arbitrary Prandtl numbers and specific heat ratios, offering a valuable tool for studying complex problems in fluid dynamics and paving the way for future extensions to the lattice Boltzmann context, by application of correction terms, as well as high-Mach and hypersonic regimes, employing target-designed reference frames.

Keywords: Kinetic model, Boltzmann equation, Bhatnagar–Gross–Krook kinetic model, double-distribution, quasi-equilibrium, Chapman–Enskog method, compressible flows, Prandtl number, Navier–Stokes–Fourier equations.

I. INTRODUCTION

Understanding compressible and high-speed fluid flows is of paramount importance for science and engineering. The development of reliable, accurate and efficient numerical methods for the simulation of compressible flows, especially on large-scale clusters, has been a topic of intense research over the past few decades [1, 2]. While different discrete approximations such as finite volumes (FVs) and finite differences (FDs) to the Navier–Stokes–Fourier (NSF) equations were the main drivers of research in that area, the advent of the lattice Boltzmann method (LBM) in the late 80’s opened the door for a new class of numerical methods rooted in the kinetic theory of gases.

Discrete velocity Boltzmann methods (DVBM), such as LBM [3, 4], solve a discrete velocity version of the Boltzmann equation [5] obtained via a finite-order expansion of the distribution function in terms of a set of orthonormal functions such as Hermite polynomials [6]. The dynamics of observable properties of a fluid described by the Euler or NSF equations are recovered in the hydrodynamic limit [7]. In addition to allowing for the possibility to include physics beyond NSF via higher-order expansions, its combination with collision models such as the Bhatnagar–Gross–Krook (BGK) approximation [8] has been shown to provide an efficient alternative to classical solvers [9, 10]. Simulation of compressible and high-speed flows with DVBM has witnessed con-

siderable advances in the past decades, illustrated most notably by formulations such as the family of unified gas kinetic scheme (UGKS) and discrete unified gas kinetic scheme (DUGKS) [11], FD and FV-based models such as those discussed in [12, 13] and the LBM [14].

In the specific context of the LBM, while research has focused primarily on the incompressible regime and stabilization of the isothermal solver through advanced collision models and entropy constrained equilibria construction [15–21], considerable advances are being reported in recent years for compressible flow simulations. These advances have been, in part, motivated by insights from kinetic theory, allowing for, e.g., proper thermal diffusivity in non-unity Prandtl number flows via models such as Shakhov [22], Holway [23] or the quasi-equilibrium (QE) approach [24–26]. The introduction of double-distribution function (DDF) models [27], where a second distribution carries the total or internal non-translational energy [28–30], had considerable impact on the development of efficient compressible LBM-based solvers capturing variable specific heat ratios. The class of DDF LBM solvers relying on standard lattices [31–35] and hybrid solvers, modeling the energy balance equation via a FD or FV solver [36] are practical illustrations of this impact. Models relying on higher-order lattices properly recovering the energy balance equation [37–39] without a need for correction terms were also developed in that context. While all these approaches relied on static quadratures and as a result were limited in terms of maximum achievable Mach number, the introduction of dynamic quadratures, starting with shifted lattices [40–42] and culminating with the particles on demand (PonD) method [43], opened the door for hypersonic flow simulations [44–48].

While the DDF approach is a necessity to model variable

^{*} Email: rubenst@ethz.ch

[†] Email: shosseini@ethz.ch

[‡] Corresponding author email: ikarlin@ethz.ch

[§] Group website: <https://ckg.ethz.ch/>

specific heat ratios, the non-unity Prandtl number can be fixed in various ways, with the QE approach offering the most flexible, generally applicable and stable realization. This has been shown in various publications, e.g. [26, 29, 31, 49, 50], focusing on the construction of a single DDF approach and/or single Prandtl number range, mostly notably $\text{Pr} \leq 1$. However, while there is ample literature covering theoretical and consistency aspects of other approaches, i.e. Holway and Shakhov, a consistent and general framework – w.r.t kinetic theory and the targeted macroscopic balance equations, i.e. NSF – combining QE and DDF, valid over all possible energy splitting approaches and Prandtl numbers, $\text{Pr} \in [0, \infty)$, is lacking in the literature. The aim of this contribution is to fill this major gap. Therefore, this paper presents a consistent kinetic modeling and discretization approach for compressible flows covering all Prandtl numbers, using the QE approach for various DDF models, extending our previous publication for $\text{Pr} = 1$ [30]. Throughout the manuscript, emphasis is placed on proper model construction, in order to correctly recover all macroscopic moments and dissipation rates for NSF level dynamics, as well as retaining strict conservation of mass, momentum and total energy.

The outline of this article is as follows: The methodology is presented in Section II, where brief background and theory is given in II A, the kinetic models are firstly described in Section II B, the results of a detailed hydrodynamic limit analysis are provided in Section II C and the models are discretized in Section II D. The physical capabilities of the constructed models are validated in terms of strict conservation, proper recovery of the NSF equations, as well as Galilean invariance, and results for two sensitive benchmarks of compressible flows with non-unity Prandtl are presented in Section III. Finally, a summary and the conclusions are provided in Section IV.

II. METHODOLOGY

A. Background

1. Boltzmann–Bhatnagar–Gross–Krook model

The Boltzmann transport equation (BE) is denoted as

$$\partial_t f(\mathbf{r}, \mathbf{v}, t) + \mathbf{v} \cdot \nabla f(\mathbf{r}, \mathbf{v}, t) = \Omega_f, \quad (1)$$

where the full Boltzmann collision integral [5] is modeled with the BGK approximation [8],

$$\Omega_f = -\frac{1}{\tau} [f(\mathbf{r}, \mathbf{v}, t) - f^{\text{eq}}(\mathbf{r}, \mathbf{v}, t)]. \quad (2)$$

Particle velocity is designated by \mathbf{v} while \mathbf{r} marks the position in space and t the time. The probability distribution function and the local equilibrium distribution function are represented by $f(\mathbf{r}, \mathbf{v}, t)$ and $f^{\text{eq}}(\mathbf{r}, \mathbf{v}, t)$, respectively. The parameter τ is the relaxation time that controls the relaxation rate of the distribution function towards the equilibrium given by the local Maxwell–Boltzmann (MB) distribution function for

monatomic particles,

$$f^{\text{eq}}(\mathbf{r}, \mathbf{v}, t) = \frac{n}{(2\pi RT)^{D/2}} \exp\left[-\frac{|\mathbf{v} - \mathbf{u}|^2}{2RT}\right], \quad (3)$$

where $n = \rho/m$ is the particle number density with the particle mass m and mass density ρ , D is the dimension of the physical space and R designates the specific gas constant. The local equilibrium distribution function is parametrized by mass density ρ , velocity \mathbf{u} and temperature T , which are found from, using the notation $v^2 = \mathbf{v} \cdot \mathbf{v}$,

$$\rho = m \int f d\mathbf{v} = m \int f^{\text{eq}} d\mathbf{v}, \quad (4)$$

$$\rho \mathbf{u} = m \int \mathbf{v} f d\mathbf{v} = m \int \mathbf{v} f^{\text{eq}} d\mathbf{v}, \quad (5)$$

$$E = m \int \frac{v^2}{2} f d\mathbf{v} = m \int \frac{v^2}{2} f^{\text{eq}} d\mathbf{v}, \quad (6)$$

where $\rho \mathbf{u}$ represents the momentum vector and E is the total energy. Thus, the temperature is obtained with the definition of the total energy for a monatomic perfect gas from the sum of the internal energy, $U^{\text{tr}} = \rho C_v^{\text{tr}} T$, and the kinetic energy, $K = \rho u^2/2$, i.e.,

$$E = U^{\text{tr}} + K = \rho C_v^{\text{tr}} T + \rho \frac{u^2}{2}, \quad (7)$$

where, due to the monatomic gas which is considered, the internal energy only contains translational modes, leading to the restriction

$$C_v^{\text{tr}} = DR/2. \quad (8)$$

For simplicity, equations are written with $m = 1$ for the remainder of this manuscript.

The MB equilibrium distribution function (EDF) annuls the Boltzmann collision integral, and is also the minimizer of the H -function,

$$H(f) = \int f \ln(f) d\mathbf{v}, \quad (9)$$

under constraints of locally conserved moments, density, momentum and total energy, i.e.,

$$f^{\text{eq}} = \operatorname{argmin} H(f) \Big|_{\rho, \rho \mathbf{u}, E}. \quad (10)$$

The BGK approximation fulfills Boltzmann's H -theorem, which states that, for solutions of the Boltzmann equation, the production of the H -function due to the collision integral is non-positive definite,

$$\sigma = \int (\ln f) \Omega_f d\mathbf{v} \leq 0, \quad (11)$$

expressing irreversible entropy production and a monotonic decay of H toward its minimum. At its minimum, which is uniquely attained at the local MB equilibrium, the H -function

is directly related to the thermodynamic entropy s of a gas through

$$s = -k_B H(f^{\text{eq}}). \quad (12)$$

The H -function may therefore be interpreted as a non-equilibrium extension of the thermodynamic entropy when the distribution function departs from the Maxwell–Boltzmann family, and the monotonic decrease of H implied by the H -theorem corresponds to non-negative entropy production in accordance with the second law of thermodynamics.

In the next section, the generic construction of quasi-equilibrium kinetic models shall be refreshed, before proceeding to a discussion of modeling general compressible flows, where the QE formalism is revisited.

2. Quasi-equilibrium kinetic models

The generic construction of QE kinetic models [24, 51] starts by denoting M as the set of locally conserved moments, i.e., Eqs. (4), (5) and (6), as

$$M(f) = \{M_0(f), \dots, M_{D+1}(f)\}, \quad (13)$$

with

$$M_k(f) = \int m_k(\mathbf{v}) f d\mathbf{v}, \quad k = 0, \dots, D+1. \quad (14)$$

The local EDF, i.e., Eq. (3), can be written as $f^{\text{eq}}(M)$, parametrized by the set of conserved moments. Furthermore, another linearly independent set of higher-order moments N can be written as

$$N(f) = \{N_0(f), \dots, N_l(f)\}, \quad (15)$$

with

$$N_k(f) = \int n_k(\mathbf{v}) f d\mathbf{v}, \quad k = 0, \dots, l. \quad (16)$$

The quasi-equilibrium distribution function (QEDF) is defined as a minimizer of the H -function, i.e., Eq. (9), subject to the fixed set of moments M and N as

$$f^*(M, N) = \operatorname{argmin} H(f) \Big|_{M, N}. \quad (17)$$

A formal solution is represented as

$$\ln f^* = \sum_{k=0}^{D+1} \lambda_k m_k + \sum_{k=0}^l \beta_k n_k, \quad (18)$$

where λ_k and β_k are Lagrange multipliers. If the solution exists, it is unique due to the convexity of the H -function. This is guaranteed if the highest-order moment $n_l \sim |\mathbf{v}|^l$ is even. By the construction, the QEDF satisfies the following consistency conditions,

$$M(f^*(M, N)) = M, \quad (19)$$

$$N(f^*(M, N)) = N, \quad (20)$$

$$f^*(M, N(f^{\text{eq}}(M))) = f^{\text{eq}}(M). \quad (21)$$

The latter condition, Eq. (21), characterizes the EDF as a special case of the QEDF.

Using BGK approximations [8], the QE kinetic model can be written as a quasi-equilibrium Bhatnagar–Gross–Krook (QE-BGK), i.e., a two-step relaxation to the equilibrium through the intermediate quasi-equilibrium state. In expanded notation this reads,

$$\begin{aligned} \Omega_f = & -\frac{1}{\tau_1}(f - f^*(M(f), N(f))) \\ & -\frac{1}{\tau_2}(f^*(M(f), N(f)) - f^{\text{eq}}(M(f))). \end{aligned} \quad (22)$$

A schematic of the BGK and the QE-BGK collision can be found in Fig. 1. Here the first stage is a relaxation from the current state f to the intermediate quasi-equilibrium f^* , with a relaxation time τ_1 , while the second stage is the relaxation from the quasi-equilibrium f^* to the equilibrium f^{eq} , with the relaxation time τ_2 . When both relaxation rates are equal, $\tau_1 = \tau_2$, the intermediate state f^* is not visited and the QE-BGK relaxation, Eq. (22), reduces to the BGK relaxation, Eq. (2). The representation of the QE kinetic model in the form of Eq. (22) can be termed sequential. Another telling form, which can be termed a parallel (see Fig. 1 for a schematic), is obtained upon rewriting Eq. (22) as

$$\begin{aligned} \Omega_f = & -\frac{1}{\tau_1}(f - f^*) - \frac{1}{\tau_2}(f^* - f^{\text{eq}}) - \frac{1}{\tau_2}f + \frac{1}{\tau_2}f^{\text{eq}} \\ = & -\left(\frac{1}{\tau_1} - \frac{1}{\tau_2}\right)(f - f^*) - \frac{1}{\tau_2}(f - f^{\text{eq}}). \end{aligned} \quad (23)$$

Here, the current state f relaxes in parallel to both the EDF, f^{eq} , (with the time τ_2) and to the intermediate QEDF, f^* . The latter relaxation is characterized with the effective relaxation time θ ,

$$\theta = \frac{\tau_1 \tau_2}{\tau_2 - \tau_1}. \quad (24)$$

Positivity of the effective relaxation time (24) requires the inequality of the relaxation times,

$$\tau_1 \leq \tau_2. \quad (25)$$

The latter hierarchy of relaxation times allows to interpret the first stage of relaxation (from f to f^*) in Eq. (22) as a "fast" process, as compared to the "slow" second stage (from f^* to f^{eq}). Consequently, the higher-order moments N are termed as slow moments, as compared to all other higher-order moments that are linearly independent from N and M . Moreover, the fundamental hierarchy of relaxation times, i.e., Eq. (25), guarantees the H -theorem for the QE kinetic models. This can be found when computing the entropy production, cf. Eq. (11), with the relaxation term in the form of Eq. (23), and

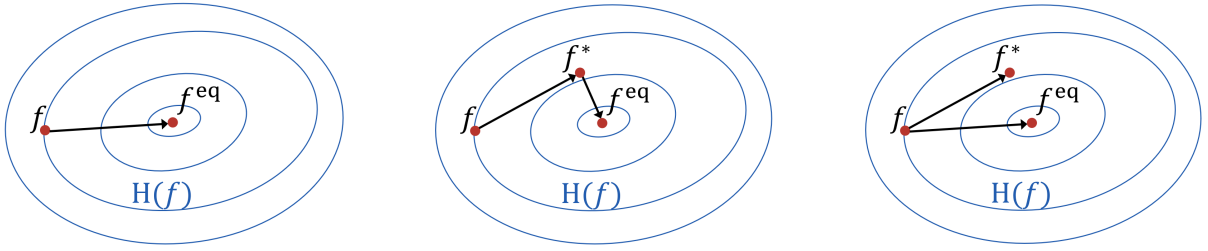


FIG. 1. Schematic of the relaxation process(es) in the BGK and QE-BGK kinetic models depicted with contour lines of the H -function. From left to right: BGK, Eq. (2); QE-BGK in serial form, Eq. (22); QE-BGK in parallel form, Eq. (23).

taking into account the inequality in Eq. (25), as

$$\begin{aligned}
 \sigma &= \int (\ln f) \Omega_f d\mathbf{v} \\
 &= - \left(\frac{1}{\tau_1} - \frac{1}{\tau_2} \right) \int (\ln f) (f - f^*) d\mathbf{v} \\
 &\quad - \frac{1}{\tau_2} \int (\ln f) (f - f^{\text{eq}}) d\mathbf{v} \\
 &= - \left(\frac{1}{\tau_1} - \frac{1}{\tau_2} \right) \int \ln \left(\frac{f}{f^*} \right) (f - f^*) d\mathbf{v} \\
 &\quad - \frac{1}{\tau_2} \int \ln \left(\frac{f}{f^{\text{eq}}} \right) (f - f^{\text{eq}}) d\mathbf{v} \\
 &\leq 0,
 \end{aligned} \tag{26}$$

where Eq. (18) was used.

In practical applications, only approximate expressions for the quasi-equilibrium distribution functions are usually available, such as Grad's moment approximation [52] or the so-called triangle entropy method [53]. However, the fundamental relaxation times hierarchy, i.e., Eq. (25), has to be maintained regardless of whether the exact quasi-equilibrium or an approximation thereof is used.

B. Kinetic model description

1. Extension to compressible flows

The Bhatnagar-Gross-Krook-Boltzmann equation (BGK-BE), as discussed in Section II A, has few well-known shortcomings that need to be addressed before being used to model general compressible flow hydrodynamics:

- Variable specific heat capacity valid for polyatomic molecules: The distribution function has to be extended in order to account for the internal roto-vibrational degrees of freedom of the gas molecules in a polyatomic gas.
- Variable Prandtl number: The BGK collision operator results in the restriction of a Prandtl number of unity.

To account for the first issue (variable specific heat capacity valid for polyatomic molecules), a widely used approach was originally introduced by Rykov [28], who extended the BGK

framework to polyatomic gases by introducing additional relaxation mechanisms to account for the additional degrees of freedom allowing to model flows with variable adiabatic exponents γ . For computational convenience, this idea was later reformulated, mainly based on the lattice Boltzmann picture, by introducing a second distribution function g , evolving according to another Boltzmann transport equation, which explicitly represents the evolution of internal roto-vibrational energy modes of the gas. This description further allowed to extend the second distribution to carry some, or the full, part of the total energy, as the g - and f -distributions can be linked to constitute the necessary information [30]. It shall be noted that, in the dilute-gas limit with monoatomic particles the double-distribution approach does not strictly reduce to the classical single-distribution BGK equation, as the conservation of energy is represented differently; this distinction does, however, not affect the recovery of the intended macroscopic hydrodynamic equations.

An option to lift the second limitation (variable Prandtl number) is given by the application of the generalized-BGK collision operator, guided by the QE approximation approach [24, 53, 54] (see previous section). The latter component decomposes the dynamics of the system into fast and slow modes, which is very practical for systems possessing different time scales of physical processes. Of interest here is a Prandtl number of non-unity,

$$\text{Pr} = \frac{C_p \mu}{\kappa} = \frac{\nu}{\alpha}, \tag{27}$$

which expresses the ratio of momentum and thermal diffusion. In the case where the heat flux is regarded as the "slow" variable, the thermal conductivity κ (or thermal diffusivity α) can be related to the "slow" relaxation time, while the dynamic (shear) viscosity μ (or kinematic viscosity ν) is proportional to the "fast" relaxation time, and vice versa.

2. Double-distribution quasi-equilibrium kinetic model

Combining the double-distribution and the QE approach, variable adiabatic exponents can be introduced and the Prandtl number can be controlled independently. The transport equa-

tions for f and g become

$$\begin{aligned} \partial_t f(\mathbf{r}, \mathbf{v}, t) + \mathbf{v} \cdot \nabla f(\mathbf{r}, \mathbf{v}, t) &= -\frac{1}{\tau_1} [f(\mathbf{r}, \mathbf{v}, t) - f^*(\mathbf{r}, \mathbf{v}, t)] \\ &\quad - \frac{1}{\tau_2} [f^*(\mathbf{r}, \mathbf{v}, t) - f^{\text{eq}}(\mathbf{r}, \mathbf{v}, t)], \end{aligned} \quad (28)$$

and

$$\begin{aligned} \partial_t g(\mathbf{r}, \mathbf{v}, t) + \mathbf{v} \cdot \nabla g(\mathbf{r}, \mathbf{v}, t) &= -\frac{1}{\tau_1} [g(\mathbf{r}, \mathbf{v}, t) - g^*(\mathbf{r}, \mathbf{v}, t)] \\ &\quad - \frac{1}{\tau_2} [g^*(\mathbf{r}, \mathbf{v}, t) - g^{\text{eq}}(\mathbf{r}, \mathbf{v}, t)]. \end{aligned} \quad (29)$$

The same consideration as in the single distribution QE model with the hierarchy of relaxation times, cf. Eq. (25), carries over to the double-distribution setting, i.e.

$$\tau_1 \leq \tau_2. \quad (30)$$

Finally, it shall be noted that the necessity of introducing an intermediate QE state when employing multiple relaxation times in the double-distribution framework has been discussed in detail in [29].

In the following sections, the construction of all EDFs and QEDFs are specified in detail.

3. Variable adiabatic exponent: Energy splits and second distribution

In the double distribution setting, the definition of the first reduced distribution function follows that of Rykov [28]. The density and momentum are computed from the first reduced distribution function, f , as

$$\rho = \int f d\mathbf{v} = \int f^{\text{eq}} d\mathbf{v}, \quad (31)$$

$$\rho \mathbf{u} = \int \mathbf{v} f d\mathbf{v} = \int \mathbf{v} f^{\text{eq}} d\mathbf{v}. \quad (32)$$

The equilibrium, f^{eq} , is defined as the MB distribution, i.e. Eq. (3), which corresponds to the minimizer of the H -function under conserved density, momentum and total energy. Therefore, the expressions (31) and (32) are the same as in Eqs. (4) and (5) used in the single-distribution case. However, the total energy, which is used in the minimization, differs from Eq. (6) and (7) in the double distribution setting, as also non-translational degrees of freedom are to be considered, which is where the second distribution comes into play. With the kinetic energy K and the full internal energy, $U = \rho C_v T$, where C_v is not anymore restricted to a monoatomic gas and thus Eq. (8), the definition of the total energy is written as

$$E = U + K = \rho C_v T + \rho \frac{u^2}{2}. \quad (33)$$

In other words, while replacing the temperature T in the Maxwell-Boltzmann equilibrium (3) through total energy as in Eq. (33) instead of Eq. (7), the reduced f^{eq} becomes

dependent on the second distribution function g , which carries parts of the additional energy due to the presence of non-translational degrees of freedom.

Different parts of energy can be carried by the second distribution, g . In this work, the forms where either the total energy or the internal non-translational energy are put on g were considered, respectively. Note that other energy splits between f and g are also possible, as can for example be read in a comparative study in [30]. However subsequent modification to Eqs. (28) and (29) leading to appearance of non-conservative and non-local source terms makes these splits less computationally attractive. In addition to that, other advantages and disadvantages were found, which will also become visible in the remainder of this manuscript. Hereafter, equations and remarks concerning uniquely the total or internal non-translational energy split are labeled by the roman numbers (I) or (II), respectively, for clearer visibility.

Using the internal energy associated with the non-translational degrees of freedom for convenience, here denoted as

$$U^{\text{nttr}} = U - U^{\text{tr}} = U - \rho \frac{DR}{2} T, \quad (34)$$

the second distribution can now be defined with respect to the total energy as

$$\begin{aligned} \text{(I)} \quad E &= \int g d\mathbf{v} = \int g^{\text{eq}} d\mathbf{v}, \\ \text{(II)} \quad E &= \int g + \frac{v^2}{2} f d\mathbf{v} = \int g^{\text{eq}} + \frac{v^2}{2} f^{\text{eq}} d\mathbf{v}, \end{aligned} \quad (35)$$

for the total and internal non-translational energy split, respectively. Consequently, the equilibrium of the second distribution is defined as

$$\begin{aligned} \text{(I)} \quad g^{\text{eq}} &= \left(\frac{U^{\text{nttr}}}{\rho} + \frac{v^2}{2} \right) f^{\text{eq}} = \left(C_v T - \frac{RDT}{2} + \frac{v^2}{2} \right) f^{\text{eq}}, \\ \text{(II)} \quad g^{\text{eq}} &= \frac{U^{\text{nttr}}}{\rho} f^{\text{eq}} = \left(C_v T - \frac{RDT}{2} \right) f^{\text{eq}}, \end{aligned} \quad (36)$$

respectively. Note that g^{eq} is therefore a reparameterization of f^{eq} .

All explicit expressions for the relevant equilibrium and conserved moments of f and g are listed in Appendix A.

4. Variable Prandtl number: Constraints for the quasi-equilibrium states

The QEDFs in the double-distribution setting are defined as the minimizer of the H -function subject to the locally conserved density, momentum and total energy and additional quasi-conserved slow fields, analogous to the single-distribution setting, cf. Eq. (17). In case of applying the QE notion to variable Prandtl numbers, the pressure tensor and the heat flux vector mark the quasi-conserved fields, with altering conditions depending on the Prandtl number $\{\text{Pr} \leq 1, \text{Pr} \geq 1\}$.

Hence, explicitly, in order to recover the NSF equations with variable Prandtl numbers, the QEDFs are required to satisfy the conservation of mass and momentum as

$$\rho = \int f^* d\mathbf{v} = \int f d\mathbf{v} = \int f^{\text{eq}} d\mathbf{v}, \quad (37)$$

$$\rho \mathbf{u} = \int \mathbf{v} f^* d\mathbf{v} = \int \mathbf{v} f d\mathbf{v} = \int \mathbf{v} f^{\text{eq}} d\mathbf{v}, \quad (38)$$

and total energy as

$$\begin{aligned} \text{(I)} \quad E &= \int g^* d\mathbf{v} = \int g d\mathbf{v} = \int g^{\text{eq}} d\mathbf{v}, \\ \text{(II)} \quad E &= \int g^* + \frac{v^2}{2} f^* d\mathbf{v} = \int g + \frac{v^2}{2} f d\mathbf{v} \\ &= \int g^{\text{eq}} + \frac{v^2}{2} f^{\text{eq}} d\mathbf{v}. \end{aligned} \quad (39)$$

For $\text{Pr} \leq 1$, in addition to Eqs. (37) to (39), the QEDFs have to satisfy for the pressure tensor,

$$\int \mathbf{v} \otimes \mathbf{v} f^* d\mathbf{v} = \int \mathbf{v} \otimes \mathbf{v} f^{\text{eq}} d\mathbf{v}, \quad (40)$$

and for the heat flux vector,

$$\begin{aligned} \text{(I)} \quad & \int \mathbf{v} g^* d\mathbf{v} - \mathbf{u} \cdot \int \mathbf{v} \otimes \mathbf{v} f^* d\mathbf{v} \\ &= \int \mathbf{v} g d\mathbf{v} - \mathbf{u} \cdot \int \mathbf{v} \otimes \mathbf{v} f d\mathbf{v}, \\ \text{(II)} \quad & \int \mathbf{v} g^* + \mathbf{v} \frac{v^2}{2} f^* d\mathbf{v} - \mathbf{u} \cdot \int \mathbf{v} \otimes \mathbf{v} f^* d\mathbf{v} \\ &= \int \mathbf{v} g + \mathbf{v} \frac{v^2}{2} f d\mathbf{v} - \mathbf{u} \cdot \int \mathbf{v} \otimes \mathbf{v} f d\mathbf{v}. \end{aligned} \quad (41)$$

For $\text{Pr} \geq 1$, the QEDFs are required to satisfy for the pressure tensor,

$$\int \mathbf{v} \otimes \mathbf{v} f^* d\mathbf{v} = \int \mathbf{v} \otimes \mathbf{v} f d\mathbf{v}, \quad (42)$$

and for the heat flux vector,

$$\begin{aligned} \text{(I)} \quad & \int \mathbf{v} g^* d\mathbf{v} - \mathbf{u} \cdot \int \mathbf{v} \otimes \mathbf{v} f^* d\mathbf{v} \\ &= \int \mathbf{v} g^{\text{eq}} d\mathbf{v} - \mathbf{u} \cdot \int \mathbf{v} \otimes \mathbf{v} f^{\text{eq}} d\mathbf{v}, \\ \text{(II)} \quad & \int \mathbf{v} g^* + \mathbf{v} \frac{v^2}{2} f^* d\mathbf{v} - \mathbf{u} \cdot \int \mathbf{v} \otimes \mathbf{v} f^* d\mathbf{v} \\ &= \int \mathbf{v} g^{\text{eq}} + \mathbf{v} \frac{v^2}{2} f^{\text{eq}} d\mathbf{v} - \mathbf{u} \cdot \int \mathbf{v} \otimes \mathbf{v} f^{\text{eq}} d\mathbf{v}. \end{aligned} \quad (43)$$

In the limit of $\text{Pr} = 1$, no quasi-conserved fields are present; only the constraints on the conserved fields hold, and thus the QEDFs are equivalent to the EDFs, i.e. $\{f^*, g^*\} = \{f^{\text{eq}}, g^{\text{eq}}\}$.

Note that the key difference in the above constraints on the quasi-conserved fields between the cases of $\text{Pr} \leq 1$ and $\text{Pr} \geq 1$, i.e. Eqs. (40) and (41) vs. Eqs. (42) and (43), lies in the QE pressure tensor and the QE heat flux vector: In one case ($\text{Pr} \leq 1$) the QE pressure tensor is set to equilibrium while the

QE heat flux is set to the full off-equilibrium distribution, whereas in the other case ($\text{Pr} \geq 1$) the QE pressure tensor is off-equilibrium and the QE heat flux is set to equilibrium. Further, note that herein, the difference in the expressions between the splits lies in the fact that the total energy E is composed of contributions from g only in the case of the total energy split, e.g. $\int g^* d\mathbf{v}$, whereas the internal non-translational energy split also contains contributions from f , e.g., $\int g^* + \frac{v^2}{2} f^* d\mathbf{v}$, cf. Eq. (39). This difference also carries over to the higher-order expressions, i.e., to the QE heat flux.

Together with the expressions for the relevant equilibrium and conserved moments in Appendix A, the specifications stated in this section (Section II B) complete all necessary information for the constructed kinetic models. Next, these models are assessed to prove convergence to a hydrodynamic limit.

C. Hydrodynamic limit

The conclusions of the multiscale analysis in the form of the Chapman-Enskog expansion [7] shall be highlighted at this point. The detailed derivations are attached in Appendix B for the interested reader. The specified system recovers the NSF equations in the hydrodynamic limit, i.e.,

$$\partial_t \rho + \nabla \cdot \rho \mathbf{u} = 0, \quad (44)$$

$$\partial_t (\rho \mathbf{u}) + \nabla \cdot (\rho \mathbf{u} \otimes \mathbf{u} + p \mathbf{I} + \boldsymbol{\tau}_{\text{NS}}) = 0, \quad (45)$$

$$\partial_t E + \nabla \cdot [(E + p) \mathbf{u} + \mathbf{q}_F + \mathbf{q}_H] = 0, \quad (46)$$

where the dissipative mechanisms are in the form of the Navier–Stokes stress tensor

$$\begin{aligned} \boldsymbol{\tau}_{\text{NS}} &= -\mu \left[\nabla \mathbf{u} + \nabla \mathbf{u}^\dagger - \frac{R}{C_v} (\nabla \cdot \mathbf{u}) \mathbf{I} \right] \\ &= -\mu \left[\nabla \mathbf{u} + \nabla \mathbf{u}^\dagger - \frac{2}{D} (\nabla \cdot \mathbf{u}) \mathbf{I} \right] - \eta (\nabla \cdot \mathbf{u}) \mathbf{I}, \end{aligned} \quad (47)$$

the Fourier heat flux

$$\mathbf{q}_F = -\kappa \nabla T, \quad (48)$$

and the viscous heating vector

$$\begin{aligned} \mathbf{q}_H &= \mathbf{u} \cdot \boldsymbol{\tau}_{\text{NS}} = -\mu \left[\mathbf{u} \cdot \nabla \mathbf{u} + \mathbf{u} \cdot \nabla \mathbf{u}^\dagger - \frac{R}{C_v} \mathbf{u} (\nabla \cdot \mathbf{u}) \right] \\ &= -\mu \left[\mathbf{u} \cdot \nabla \mathbf{u} + \mathbf{u} \cdot \nabla \mathbf{u}^\dagger - \frac{2}{D} \mathbf{u} (\nabla \cdot \mathbf{u}) \right] - \eta \mathbf{u} (\nabla \cdot \mathbf{u}). \end{aligned} \quad (49)$$

From the multiscale analysis it is further found that the relaxation parameters τ_1 and τ_2 in Eqs. (28) and (29) are related to the shear viscosity μ , bulk viscosity η and thermal conductivity κ as, for $\text{Pr} \leq 1$,

$$v = \frac{\mu}{\rho} = \tau_1 RT, \quad (50)$$

$$\zeta = \frac{\eta}{\rho} = \left(\frac{2}{D} - \frac{R}{C_v} \right) \tau_1 RT, \quad (51)$$

$$\alpha = \frac{\kappa}{C_p \rho} = \tau_2 RT, \quad (52)$$

while for $\text{Pr} \geq 1$

$$v = \frac{\mu}{\rho} = \tau_2 RT, \quad (53)$$

$$\zeta = \frac{\eta}{\rho} = \left(\frac{2}{D} - \frac{R}{C_v} \right) \tau_2 RT, \quad (54)$$

$$\alpha = \frac{\kappa}{C_p \rho} = \tau_1 RT, \quad (55)$$

and can therefore be found from the imposed dynamic shear viscosity and Prandtl number. In order to respect the relaxation times hierarchy, cf. Eq. (30), it becomes evident that the Prandtl number and the relaxation parameters are related through

$$\text{Pr} = \begin{cases} \frac{\tau_1}{\tau_2}, & \text{Pr} \leq 1, \\ \frac{\tau_2}{\tau_1}, & \text{Pr} \geq 1. \end{cases} \quad (56)$$

Next, the discretization of the model in phase space is discussed.

D. Phase-space discretization

1. Discrete velocity system

The phase-space is discretized with a set of Q discrete velocities \mathbf{v}_i , where $i \in \{0, Q-1\}$. Discretization is operated via expansion using the Hermite orthonormal polynomials and application of the Gauss-Hermite quadrature. As this is standard practice, further description is omitted here for the sake of readability, however, the interested reader can find more details in Appendix C or refer to [3, 6]. The phase-space-discrete system of hyperbolic partial differential equations (PDEs) then reads,

$$\begin{aligned} \partial_t f_i(\mathbf{r}, t) + \mathbf{v}_i \cdot \nabla f_i(\mathbf{r}, t) &= -\frac{1}{\tau_1} [f_i(\mathbf{r}, t) - f_i^*(\mathbf{r}, t)] \\ &\quad - \frac{1}{\tau_2} [f_i^*(\mathbf{r}, t) - f_i^{\text{eq}}(\mathbf{r}, t)]. \end{aligned} \quad (57)$$

and,

$$\begin{aligned} \partial_t g_i(\mathbf{r}, t) + \mathbf{v}_i \cdot \nabla g_i(\mathbf{r}, t) &= -\frac{1}{\tau_1} [g_i(\mathbf{r}, t) - g_i^*(\mathbf{r}, t)] \\ &\quad - \frac{1}{\tau_2} [g_i^*(\mathbf{r}, t) - g_i^{\text{eq}}(\mathbf{r}, t)]. \end{aligned} \quad (58)$$

Moments of distribution functions are computed as numerical quadratures, e.g. the conserved density and momentum as

$$\rho = \sum_{i=0}^{Q-1} f_i = \sum_{i=0}^{Q-1} f_i^{\text{eq}} = \sum_{i=0}^{Q-1} f_i^*, \quad (59)$$

$$\rho \mathbf{u} = \sum_{i=0}^{Q-1} \mathbf{v}_i f_i = \sum_{i=0}^{Q-1} \mathbf{v}_i f_i^{\text{eq}} = \sum_{i=0}^{Q-1} \mathbf{v}_i f_i^*, \quad (60)$$

and total energy as

$$\begin{aligned} \text{(I)} \quad E &= \sum_{i=0}^{Q-1} g_i = \sum_{i=0}^{Q-1} g_i^{\text{eq}} = \sum_{i=0}^{Q-1} g_i^*, \\ \text{(II)} \quad E &= \sum_{i=0}^{Q-1} g_i + \frac{v_i^2}{2} f_i = \sum_{i=0}^{Q-1} g_i^{\text{eq}} + \frac{v_i^2}{2} f_i^{\text{eq}} = \sum_{i=0}^{Q-1} g_i^* + \frac{v_i^2}{2} f_i^*. \end{aligned} \quad (61)$$

2. Discrete equilibria

The discrete f - and g -equilibria can be reconstructed as a finite-order Grad expansion [52],

$$f_i^{\text{eq}} = w_i \sum_{n=0}^N \frac{1}{n! (RT_{\text{ref}})^n} \mathbf{a}_n^{\text{eq}}(f) : \mathcal{H}_n(\mathbf{v}_i), \quad (62)$$

$$g_i^{\text{eq}} = w_i \sum_{n=0}^N \frac{1}{n! (RT_{\text{ref}})^n} \mathbf{a}_n^{\text{eq}}(g) : \mathcal{H}_n(\mathbf{v}_i), \quad (63)$$

where the series is truncated at the order N . The weights and the reference temperature of the velocity set are given by w_i and T_{ref} , respectively. Both discrete equilibria are written as expansions parametrized by $\mathcal{H}_n(\mathbf{v}_i)$ and $\mathbf{a}_n(\{f, g\})$, where $\mathcal{H}_n(\mathbf{v}_i)$ is the Hermite polynomial tensor of order n of the i -th particle velocity and \mathbf{a}_n is the corresponding coefficient tensor accounting for the required set of equilibrium moments. More details and the explicit expressions for the Hermite polynomials and coefficients of the Grad expansion are given in Appendix D. The set of equilibrium moments can directly be drawn from Appendix A.

3. Requirements on the phase-space discretization

When going from a continuous phase-space to a discrete velocity set, there are a minimum number of requirements that need to be satisfied. To capture the fundamental flow physical properties of the NSF equations in the hydrodynamic limit, all moments appearing in the phase-space continuous multi-scale expansion have to be matched when computed with discrete quadratures. The detailed considerations can be found in Appendix E. In summary, for the f -distribution, equilibrium moments up to order three have to be properly recovered for the total energy split. For the non-translational energy split, fourth-order equilibrium moments have to be properly recovered as well. For the g -distribution, regardless of the split, equilibrium moments up to order two need to be properly recovered. These orders of expansion require higher-order velocity sets, cf. [38] or standard nearest-neighbor velocity sets with correction terms to the otherwise incorrectly recovered higher-order moments [31, 50].

Note that the discrete g -equilibria, if applied with the same velocity set as f , can also be directly parametrized by the discrete f -equilibria as in the phase-space continuous kinetic model, cf. Eq. (36). The detailed considerations can be

found in Appendix F. In summary, while this parametrization simplifies the computation of the g_i^{eq} for the internal non-translational energy split, for the total energy split it increases the orders of the Grad expansion and the quadrature.

In this work, all equilibria were constructed with the Grad–Hermite expansion and the solution via higher-order velocity sets was considered. The direct parametrization of g_i was not considered, in order to apply the minimal Hermite-based higher-order velocity sets (in two dimensions), i.e., the D2Q16 and the D2Q25 were used for the total and internal non-translational energy splits, respectively. The details of the mentioned velocity sets are listed in Appendix G.

4. Discrete quasi-equilibria

Finally, the construction of the QE-populations remains to be clarified. They are also constructed using the Grad–Hermite expansion to the same order as discussed before. However, a different set of moments is accounted for in the coefficient tensors $\mathbf{a}_n^*(\{f, g\})$. Due to the similarity in the derivation of equilibria (minimization of discrete H -function under constraints of the conserved moments, cf. constraints in Eqs. (37) to (39)), the quasi-equilibria generally contain the equilibrium moments with the exception of some moments coming from the constraints for the quasi-conserved fields, i.e. Eqs. (40) to (43). This means that the quasi-equilibria can be constructed as a "new" Grad–Hermite expansion, or as a "modification" to the computed equilibrium populations at the affected order. To be concise, the full expansions of all distributions are used herein. For this, the QE moments to use in the coefficient tensors are as follows.

For $\text{Pr} < 1$, one has

$$(I, II) \quad \sum_{i=0}^{Q-1} \mathbf{v}_i \otimes \mathbf{v}_i f_i^* = \sum_{i=0}^{Q-1} \mathbf{v}_i \otimes \mathbf{v}_i f_i^{\text{eq}}, \quad (64)$$

for both splits. In addition, for the total energy split one obtains

$$(I) \quad \sum_{i=0}^{Q-1} \mathbf{v}_i g_i^* = \sum_{i=0}^{Q-1} \mathbf{v}_i g_i - \mathbf{u} \cdot \left(\sum_{i=0}^{Q-1} \mathbf{v}_i \otimes \mathbf{v}_i f_i - \sum_{i=0}^{Q-1} \mathbf{v}_i \otimes \mathbf{v}_i f_i^{\text{eq}} \right), \quad (65)$$

and for the internal non-translational energy split, the explicit expressions read

$$(II) \quad \sum_{i=0}^{Q-1} \mathbf{v}_i g_i^* = \sum_{i=0}^{Q-1} \mathbf{v}_i g_i, \quad (66)$$

and

$$(II) \quad \sum_{i=0}^{Q-1} \mathbf{v}_i \otimes \mathbf{v}_i \otimes \mathbf{v}_i f_i^* = \sum_{i=0}^{Q-1} \mathbf{v}_i \otimes \mathbf{v}_i \otimes \mathbf{v}_i f_i - 2\mathbf{u} \otimes \left(\sum_{i=0}^{Q-1} \mathbf{v}_i \otimes \mathbf{v}_i f_i - \sum_{i=0}^{Q-1} \mathbf{v}_i \otimes \mathbf{v}_i f_i^{\text{eq}} \right), \quad (67)$$

where Eq. (64) was applied. The latter expression for the third-order moment of f^* is slightly over-constrained, as in

[55]. For $\text{Pr} > 1$, one has

$$(I) \quad \sum_{i=0}^{Q-1} \mathbf{v}_i \otimes \mathbf{v}_i f_i^* = \sum_{i=0}^{Q-1} \mathbf{v}_i \otimes \mathbf{v}_i f_i, \quad (68)$$

for the total energy split, whereas for the internal non-translational split one obtains

$$(II) \quad \sum_{i=0}^{Q-1} \mathbf{v}_i \otimes \mathbf{v}_i f_i^* = \sum_{i=0}^{Q-1} \mathbf{v}_i \otimes \mathbf{v}_i f_i - \frac{\mathbf{I}}{D} \sum_{i=0}^{Q-1} v_i^2 (f_i - f_i^{\text{eq}}), \quad (69)$$

in order to respect Eq. (61) (conservation of total energy) at the same time. Additionally, for the total energy split one obtains and

$$(I) \quad \sum_{i=0}^{Q-1} \mathbf{v}_i g_i^* = \sum_{i=0}^{Q-1} \mathbf{v}_i g_i^{\text{eq}} + \mathbf{u} \cdot \left(\sum_{i=0}^{Q-1} \mathbf{v}_i \otimes \mathbf{v}_i f_i - \sum_{i=0}^{Q-1} \mathbf{v}_i \otimes \mathbf{v}_i f_i^{\text{eq}} \right), \quad (70)$$

and for the internal on-translational split the explicit expressions are

$$(II) \quad \sum_{i=0}^{Q-1} \mathbf{v}_i g_i^* = \sum_{i=0}^{Q-1} \mathbf{v}_i g_i^{\text{eq}}, \quad (71)$$

and

$$(II) \quad \sum_{i=0}^{Q-1} \mathbf{v}_i \otimes \mathbf{v}_i \otimes \mathbf{v}_i f_i^* = \sum_{i=0}^{Q-1} \mathbf{v}_i \otimes \mathbf{v}_i \otimes \mathbf{v}_i f_i^{\text{eq}} + 2\mathbf{u} \otimes \left(\sum_{i=0}^{Q-1} \mathbf{v}_i \otimes \mathbf{v}_i (f_i - f_i^{\text{eq}}) - \frac{\mathbf{I}}{D} \sum_{i=0}^{Q-1} v_i^2 (f_i - f_i^{\text{eq}}) \right). \quad (72)$$

where Eq. (68) was applied. The latter expression for the third-order moment of f^* is again slightly over-constrained, as in [55]. Note that all above expressions satisfy the constraints in Eqs. (37) to (43).

Further, note that the derived conditions can also be formulated in another Hermite basis, for example with \mathcal{H}_{xy} , $\mathcal{H}_{xx} - \mathcal{H}_{yy}$ and $\mathcal{H}_{xx} + \mathcal{H}_{yy}$ in the second-order contributions for the Grad expansions, in order to impose conditions on the trace and traceless parts of the second-order moments directly, which could be useful for, e.g., incorporating a contacted moment.

5. Summary of the discrete equilibria and quasi-equilibria construction

A summary of the construction of all discrete equilibria and quasi-equilibria can be found in Table I. The expressions for the equilibrium moments can be drawn from Appendix A. All expressions that differ from the equilibria construction are indicated with colored background. The following notation is

(I) Total energy split							
Prandtl	Pop.	Set of moments					Comment
any	f_i^{eq}	$M_0(f^{\text{eq}}), \mathbf{M}_1(f^{\text{eq}}),$	$\mathbf{M}_2(f^{\text{eq}}),$	$\mathbf{M}_3(f^{\text{eq}}),$	-	-	
	g_i^{eq}	$M_0(g^{\text{eq}}), \mathbf{M}_1(g^{\text{eq}}),$	$\mathbf{M}_2(g^{\text{eq}}),$	-	-	-	
Pr = 1	f_i^*	$M_0(f^{\text{eq}}), \mathbf{M}_1(f^{\text{eq}}),$	$\mathbf{M}_2(f^{\text{eq}}),$	$\mathbf{M}_3(f^{\text{eq}}),$	-	$f_i^* = f_i^{\text{eq}}$	
	g_i^*	$M_0(g^{\text{eq}}), \mathbf{M}_1(g^{\text{eq}}),$	$\mathbf{M}_2(g^{\text{eq}}),$	-	-	$g_i^* = g_i^{\text{eq}}$	
Pr < 1	f_i^*	$M_0(f^{\text{eq}}), \mathbf{M}_1(f^{\text{eq}}),$	$\mathbf{M}_2(f^{\text{eq}}),$	$\mathbf{M}_3(f^{\text{eq}}),$	-	$f_i^* = f_i^{\text{eq}}$	
	g_i^*	$M_0(g^{\text{eq}}), \mathbf{M}_1(g) - \mathbf{u} \cdot (\mathbf{M}_2(f) - \mathbf{M}_2(f^{\text{eq}})),$	$\mathbf{M}_2(g^{\text{eq}}),$	-	-	-	
Pr > 1	f_i^*	$M_0(f^{\text{eq}}), \mathbf{M}_1(f^{\text{eq}}),$	$\mathbf{M}_2(f),$	$\mathbf{M}_3(f^{\text{eq}}),$	-	-	
	g_i^*	$M_0(g^{\text{eq}}), \mathbf{M}_1(g^{\text{eq}}) + \mathbf{u} \cdot (\mathbf{M}_2(f) - \mathbf{M}_2(f^{\text{eq}})),$	$\mathbf{M}_2(g^{\text{eq}}),$	-	-	-	
(II) Internal non-translational energy split							
Prandtl	Pop.	Set of moments					Comment
any	f_i^{eq}	$M_0(f^{\text{eq}}), \mathbf{M}_1(f^{\text{eq}}),$	$\mathbf{M}_2(f^{\text{eq}}),$	$\mathbf{M}_3(f^{\text{eq}}),$	$\mathbf{M}_4(f^{\text{eq}})$	-	
	g_i^{eq}	$M_0(g^{\text{eq}}), \mathbf{M}_1(g^{\text{eq}}),$	$\mathbf{M}_2(g^{\text{eq}}),$	-	-	-	
Pr = 1	f_i^*	$M_0(f^{\text{eq}}), \mathbf{M}_1(f^{\text{eq}}),$	$\mathbf{M}_2(f^{\text{eq}}),$	$\mathbf{M}_3(f^{\text{eq}}),$	$\mathbf{M}_4(f^{\text{eq}})$	$f_i^* = f_i^{\text{eq}}$	
	g_i^*	$M_0(g^{\text{eq}}), \mathbf{M}_1(g^{\text{eq}}),$	$\mathbf{M}_2(g^{\text{eq}}),$	-	-	$g_i^* = g_i^{\text{eq}}$	
Pr < 1	f_i^*	$M_0(f^{\text{eq}}), \mathbf{M}_1(f^{\text{eq}}),$	$\mathbf{M}_2(f^{\text{eq}}),$	$\mathbf{M}_3(f) - 2\mathbf{u} \otimes (\mathbf{M}_2(f) - \mathbf{M}_2(f^{\text{eq}})),$	$\mathbf{M}_4(f^{\text{eq}})$	-	
	g_i^*	$M_0(g^{\text{eq}}), \mathbf{M}_1(g),$	$\mathbf{M}_2(g^{\text{eq}}),$	-	-	-	
Pr > 1	f_i^*	$M_0(f^{\text{eq}}), \mathbf{M}_1(f^{\text{eq}}),$	$\mathbf{M}_2(f) - \frac{1}{D} \text{tr}(\mathbf{M}_2(f) - \mathbf{M}_2(f^{\text{eq}})),$	$\mathbf{M}_3(f^{\text{eq}}) + 2\mathbf{u} \otimes [(\mathbf{M}_2(f) - \mathbf{M}_2(f^{\text{eq}})) - \frac{1}{D} \text{tr}(\mathbf{M}_2(f) - \mathbf{M}_2(f^{\text{eq}}))],$	$\mathbf{M}_4(f^{\text{eq}})$	-	
	g_i^*	$M_0(g^{\text{eq}}), \mathbf{M}_1(g^{\text{eq}}),$	$\mathbf{M}_2(g^{\text{eq}}),$	-	-	$g_i^* = g_i^{\text{eq}}$	

TABLE I. Summary of moments for the construction of equilibrium and quasi-equilibrium populations using Grad–Hermite expansions.

used in the table,

$$\mathbf{M}_n(\{f, g\}) = \sum_{i=0}^{Q-1} \overbrace{v_i \otimes \cdots \otimes v_i}^n \{f_i, g_i\}, \quad (73)$$

$$\mathbf{M}_n(\{f^{\text{eq}}, g^{\text{eq}}\}) = \sum_{i=0}^{Q-1} \overbrace{v_i \otimes \cdots \otimes v_i}^n \{f_i^{\text{eq}}, g_i^{\text{eq}}\}. \quad (74)$$

III. VALIDATION, RESULTS AND DISCUSSION

A. Discrete velocity Boltzmann implementation

1. Time-explicit finite-volume scheme

As the Hermite-based higher-order velocity sets employed in this work do not propagate on-lattice, instead of using a semi-Lagrangian approach, e.g. [56–59], a time-explicit finite-volume scheme in the form of a discrete velocity Boltzmann solver is used for the fully conservative discretization in space and time, similar as in Strässle et al. [39], Ji et al. [48]. For simplicity, a first-order Euler-forward discretization in time was applied. Note that the resulting distribution functions and moments should be understood as volumetric averages over a cell. The resulting fully discretized system of hyperbolic PDEs are written as

$$\begin{aligned} \{f_i, g_i\}(\mathbf{r}, t + \delta t) &= \{f_i, g_i\}(\mathbf{r}, t) - \frac{\delta t}{\delta V} \sum_{\sigma \in \Theta} \{\mathcal{F}_i, \mathcal{G}_i\}(\sigma, t) \\ &\quad - \frac{\delta t}{\tau_1} \left[\{f_i, g_i\}(\mathbf{r}, t) - \{f_i^*, g_i^*\}(\mathbf{r}, t) \right] \\ &\quad - \frac{\delta t}{\tau_2} \left[\{f_i^*, g_i^*\}(\mathbf{r}, t) - \{f_i^{\text{eq}}, g_i^{\text{eq}}\}(\mathbf{r}, t) \right]. \end{aligned} \quad (75)$$

Here δt is the time-step size, δV the volume of the cell and $\{\mathcal{F}_i, \mathcal{G}_i\}$ fluxes through cell boundaries σ . The estimation of

the fluxes through the cell boundaries is the key ingredient in the discretization of space, both in terms of accuracy and stability.

2. Flux reconstruction

The fluxes in Eq. (75) are computed as

$$\{\mathcal{F}_i, \mathcal{G}_i\}(\sigma) = \mathbf{v}_i \cdot \mathbf{n}(\sigma) \{f_i, g_i\}(\sigma) \delta A(\sigma), \quad (76)$$

where \mathbf{n} is the surface normal vector and δA the infinitesimal area of the discrete surface σ of the Cuboid's hull Θ with volume δV . The distribution functions require interpolation to the interfaces in an accurate, yet stable, manner by introducing more numerical dissipation if necessary. In this work, a nearest neighbor deformation (NND) interpolation scheme [60, 61] was applied together with a generalized van Leer limiter [62], which takes into account the ratio of successive slopes a, b [63, 64]. On a uniform Cartesian grid, the scheme reads

$$\begin{aligned} v_{i,x-\delta x/2} \geq 0: \{f_i, g_i\}_{x-\delta x/2} &= \{f_i, g_i\}_{x-\delta x} + \frac{b}{2} \phi(a, b); \\ a &= \{f_i, g_i\}_{x-\delta x} - \{f_i, g_i\}_{x-2\delta x}, \\ b &= \{f_i, g_i\}_x - \{f_i, g_i\}_{x-\delta x}, \\ v_{i,x-\delta x/2} < 0: \{f_i, g_i\}_{x-\delta x/2} &= \{f_i, g_i\}_x + \frac{b}{2} \phi(a, b); \\ a &= \{f_i, g_i\}_x - \{f_i, g_i\}_{x+\delta x}, \\ b &= \{f_i, g_i\}_{x-\delta x} - \{f_i, g_i\}_x, \end{aligned} \quad (77)$$

here denoted only for the discrete surface located at $\sigma = x - \delta x/2$, with

$$\phi(a, b) = \max \left(0, \min \left[\beta \frac{a}{b}, \frac{1}{2} \left(1 + \frac{a}{b} \right), \beta \right] \right); \quad \beta \in [1, 2], \quad (78)$$

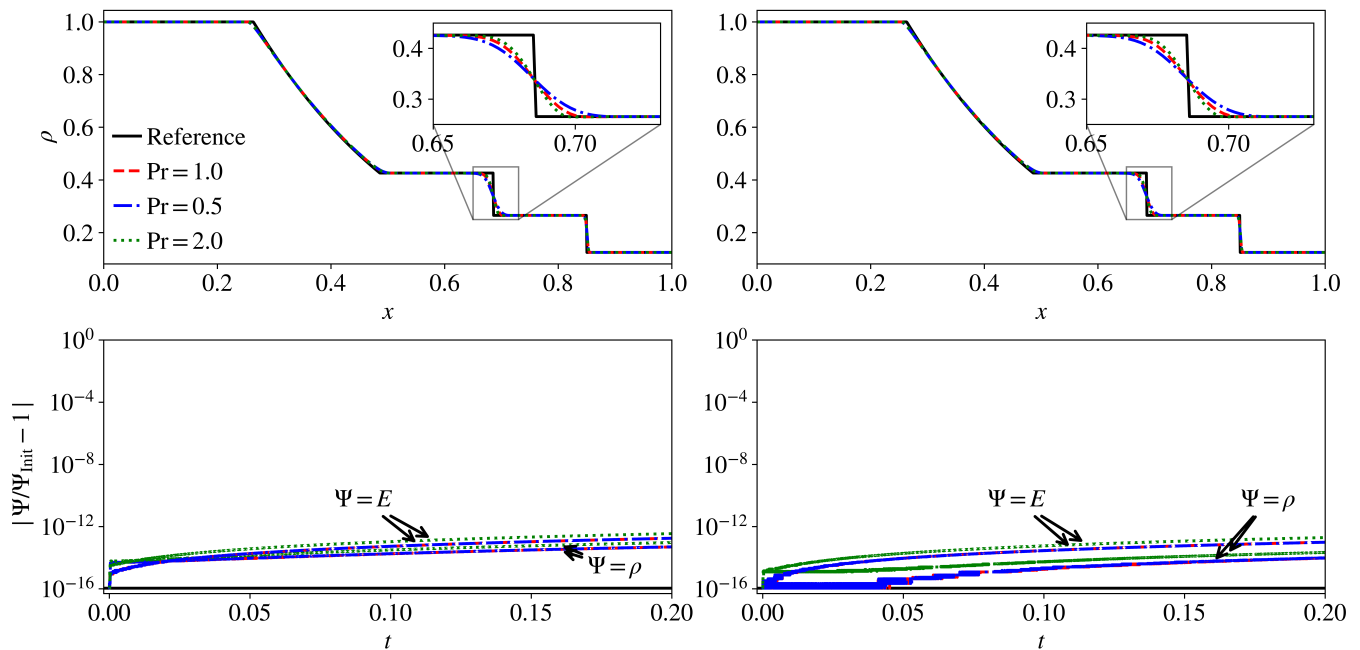


FIG. 2. Results of the shock tube problem with $Pr = \{0.5, 1, 2\}$ for the total energy split in the left column and internal-non-translational in the right column. The top row depicts a comparison of the density with the reference (Riemann solution for inviscid problem), whereas the bottom row shows the relative error in conservation of mass and total energy, where the machine epsilon for double precision is depicted as a reference.

where a free parameter of $\beta = 1$ would lead to the most dissipation, reducing the limiter to a classical minmod.

3. Simulation parameters

In all simulations, unless otherwise stated, the parameters for the presented results were set to $\mu = 5 \times 10^{-5}$ and $\gamma = 1.4$ with the gas constant set to $R = 1$. The cases were run to solve for the NSF solution, i.e. the requirements outlined in Section IID 3 concerning the Grad expansion and the quadrature order of the velocity set were respected such that the NSF equations are recovered in the hydrodynamic limit. The free parameter in the flux limiter was set to $\beta = 1.2$. Initial conditions (ICs) were supplied by means of equilibrium populations. 1-D tests were run as pseudo 1-D with periodic boundary conditions (BCs) in the pseudo direction, otherwise von Neumann BCs were applied. The time step was estimated with

$$\delta t = \frac{\min(\delta x, \delta y)}{|\mathbf{u}| + c_s} \text{CFL}, \quad (79)$$

where the CFL number was uniformly set to 0.01 in order to also stably simulate higher Mach numbers. Physical quantities are reported as non-dimensional values whenever no units are mentioned.

B. Conservation properties

First, the conservation properties of the discrete kinetic models were addressed. This was tested using a Sod shock tube [65] with the ICs

$$(\rho, p, u_x) = \begin{cases} (1, 1, 0), & 0 \leq x \leq 0.5, \\ (0.125, 0.1, 0), & 0.5 < x \leq 1, \end{cases} \quad (80)$$

in an extended fully periodic domain, $x \in [-0.5, 1.5]$. A spatial resolution of $\delta x = L_x/1024$ was applied such that the relevant region in $x \in [0, 1]$ contains 512 cells.

The results for the cropped region $x \in [0, 1]$ at $t = 0.2\text{s}$ are depicted in Fig. 2 (top row) together with the reference obtained from the Riemann solution of the inviscid problem. The relative errors in conservation of mass and total energy in the total domain are shown in the bottom row. All models (total and internal non-translational energy split for Prandtl number $Pr = \{0.5, 1, 2\}$) capture the reference solution with good agreement. The same conservation errors, which are in the order of the rounding machine precision ($2^{-53} \approx 1.11 \times 10^{-16}$ for double precision) on each cell interface, are achieved for all models, hence it is apparent that all constructed models are strictly conservative. Further, it can be seen that the dissipation around the shocks slightly change for $Pr = \{0.5, 1, 2\}$, however, importantly, the positions of all characteristic waves in this problem (shock, contact discontinuity and rarefaction wave) do not depend on the Prandtl number. This further confirms the models' correctness, as the position of these waves is determined by the Euler level solution, i.e. the dispersion of

the hydrodynamic modes and the speed of sound, which are not affected by the dissipation of hydrodynamic modes such as the Prandtl-dependent thermal dissipation rate. The dispersion and dissipation of hydrodynamic modes are therefore validated next for a variety of imposed parameters.

C. Dispersion of hydrodynamic modes: Speed of sound

The dispersion rates were probed to further assess the correct behavior concerning dispersion of hydrodynamic eigenmodes. For this, a standard test was used as, e.g., given in [30, 32, 33, 39, 48]. Note that all results reported here correspond to converged simulations in space and time. All setups were run in a fully periodic pseudo 1-D domain $x \in [0, 1]$ with a resolution of $\delta x = L_x/512$.

The temperature dependence of the speed of sound was investigated by means of a freely traveling pressure front. To that end, the domain was divided into two regions with

$$p = \begin{cases} 1 + A, & 0 \leq x \leq 0.5, \\ 1, & 0.5 < x \leq 1, \end{cases} \quad (81)$$

with amplitude $A = 1 \times 10^{-6}$. A uniform temperature $T = T_0$ as well as velocity $u_x = u_0$ was applied in both regions. The velocity was derived from the Mach number as $u_0 = \text{Ma} \sqrt{\gamma R T_0}$ and varied in subsequent simulations. Two different specific heat ratios, namely $\gamma = 5/3$ and $\gamma = 8/6$, were assessed for various temperatures. The speed of sound was computed by tracking the shock front relative to the mean flow velocity $u_x = u_0$ over time and comparing it with the analytical value of $c_s = \sqrt{\gamma R T}$.

Fig. 3 demonstrates that all constructed models for different specific heat ratios and Prandtl numbers can correctly capture the speed of sound over a wide temperature range spanning four orders of magnitude with the total energy split and three orders of magnitude with the internal non-translational split, respectively. The same applies over a wide Mach number range up to $\text{Ma} \approx 3.0$, for both energy splits, where deviations eventually start occurring due to spurious numerical oscillations.

The difference in the reported range of temperature is tied to the stability limits associated to the employed velocity sets. It is known that the D2Q16, which was employed with the total energy split, possesses an increased temperature range as compared to the D2Q25 velocity set, which was employed with the internal non-translational split. These results confirm that the models were correctly constructed for what concerns the Euler level solutions and dispersion of eigenmodes.

D. Dissipation of hydrodynamic modes: Shear, bulk and entropic modes

To further assess the correct behavior concerning dissipation of hydrodynamic eigenmodes, the dissipation rates, i.e. shear, normal and entropic, were probed. For this, standard tests were used as, e.g., given in [30, 32, 33, 39, 48]. Note

that all results reported here correspond to converged simulations in space and time. All setups were run in a fully periodic pseudo 1-D domain $x \in [0, 1]$ with a resolution of $\delta x = L_x/512$.

1. Shear viscosity

The kinematic shear viscosity ν was investigated by simulating a plane shear wave with a small sinusoidal perturbation superimposed to the initial velocity field. The ICs read

$$\rho = \rho_0, T = T_0, u_x = u_0, u_y = A \sin(2\pi x/L_x), \quad (82)$$

where the initial density and temperature were set to $(\rho_0, T_0) = (1, 1)$. The perturbation amplitude was $A = 1 \times 10^{-6}$ and u_0 , which is derived from the Mach number as $u_0 = \text{Ma} \sqrt{\gamma R T_0}$, was varied in subsequent simulations. The evolution of the maximum velocity u_y^{\max} in the domain was tracked over time and an exponential function was fitted to it. The decay rate, i.e. the shear viscosity ν , was then obtained via

$$u_y^{\max}(t) \propto \exp\left(-\frac{4\pi^2 \nu}{L_x^2} t\right). \quad (83)$$

The obtained results are depicted in Fig. 4. The measured viscosities are in excellent agreement with the imposed values and recover the expression from the Chapman-Enskog analysis, cf. Section II C, for several Ma numbers.

2. Bulk viscosity

The kinematic bulk viscosity ζ was investigated via the decay rate of sound waves in the linear regime. For this purpose, a small perturbation with initial amplitude $A = 1 \times 10^{-6}$ was superimposed to the density field. The flow was initialized as

$$\rho = \rho_0 + A \sin(2\pi x/L_x), T = T_0, u_x = u_0, u_y = 0, \quad (84)$$

with $(\rho_0, T_0) = (1, 1)$ and u_0 derived from the imposed Mach number. The perturbation acoustic energy $E'(t) = u_x^2 + u_y^2 - u_0^2 + c_s^2 \rho'^2$ of the whole domain, with $\rho' = \rho - \rho_0$, was tracked over time and the exponential function,

$$E'(t) \propto \exp\left(-\frac{4\pi^2 \nu_e}{L_x^2} t\right), \quad (85)$$

as defined by [66], was fitted to it. The recovered decay rate is the effective viscosity ν_e , i.e. the combination of shear and bulk viscosities as

$$\nu_e = \frac{4}{3} \nu + \zeta. \quad (86)$$

The obtained results are depicted in Fig. 5 for several imposed viscosities and specific heat ratios at various Ma numbers. It can be seen that the measured bulk viscosities accurately recover the expression from the Chapman-Enskog analysis, cf. Section II C, for all models.

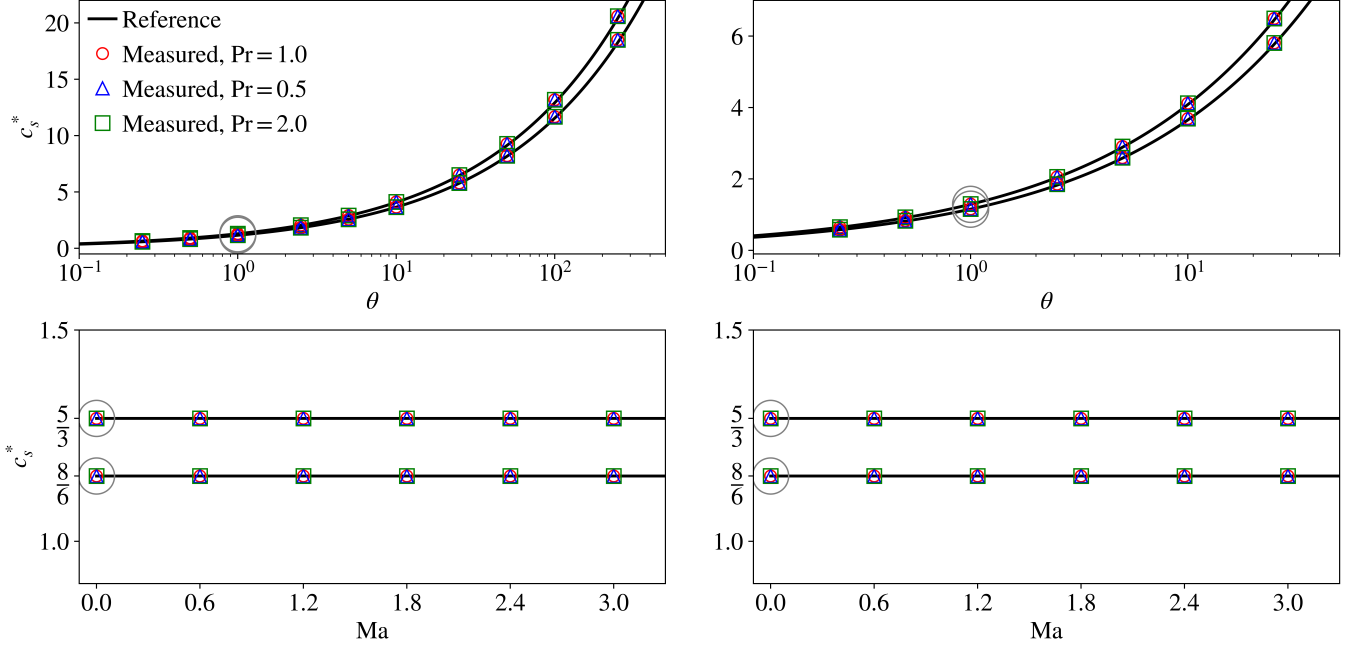


FIG. 3. Results of the dispersion tests with $\gamma = \{5/3, 8/6\}$ and $Pr = \{0.5, 1, 2\}$ for the total energy split in the left column and internal-non-translational in the right column. The top row depicts a comparison of the measured normalized speed of sound $c_s^* = \sqrt{\gamma R \theta}$ at various normalized temperatures $\theta = T/T_{ref}$ for $Ma = 0$, i.e. $u_x = u_0 = 0$, whereas the bottom row shows c_s^* at various Mach numbers of the mean flow at $\theta = 1$, i.e. $T = T_0 = T_{ref}$. The gray circles indicate corresponding measurement points between the two rows.

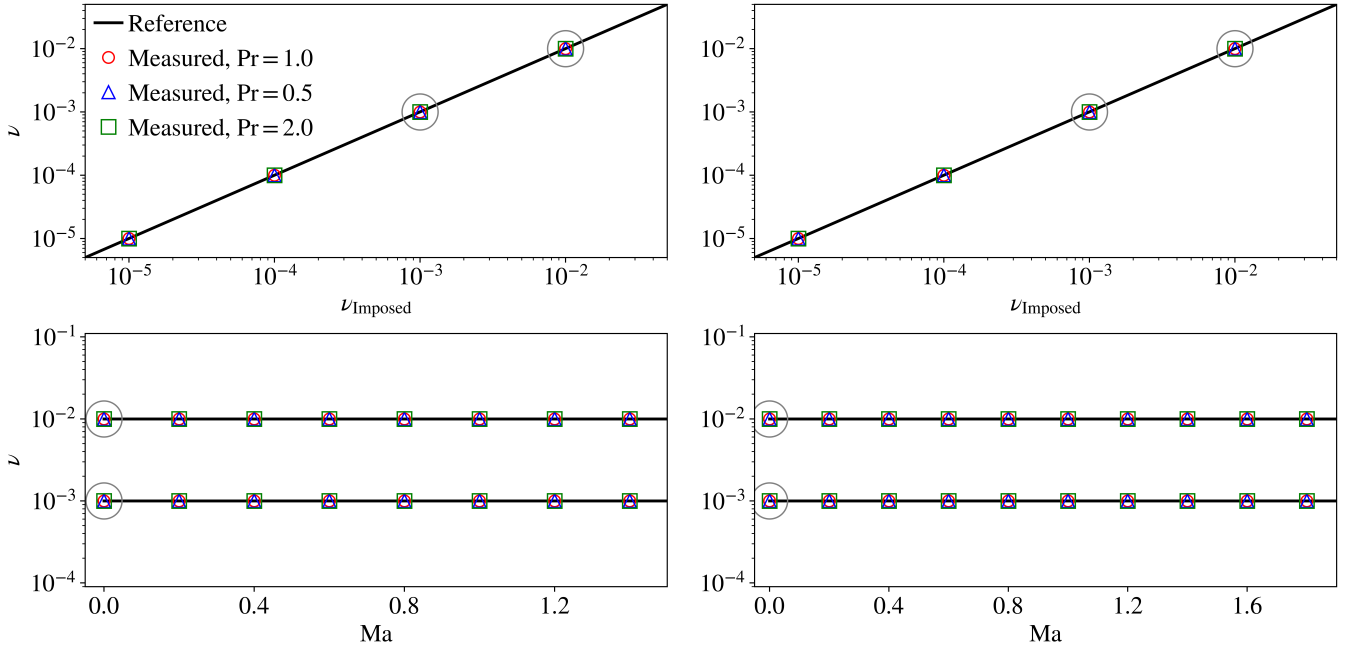


FIG. 4. Results of the dissipation tests for the shear mode with $Pr = \{0.5, 1, 2\}$ for the total energy split in the left column and internal-non-translational in the right column. The measured versus imposed values of kinematic shear viscosity is depicted in the top row at $Ma = 0$, whereas the bottom row shows the measured values at various Mach numbers. The gray circles indicate corresponding measurement points between the two rows.

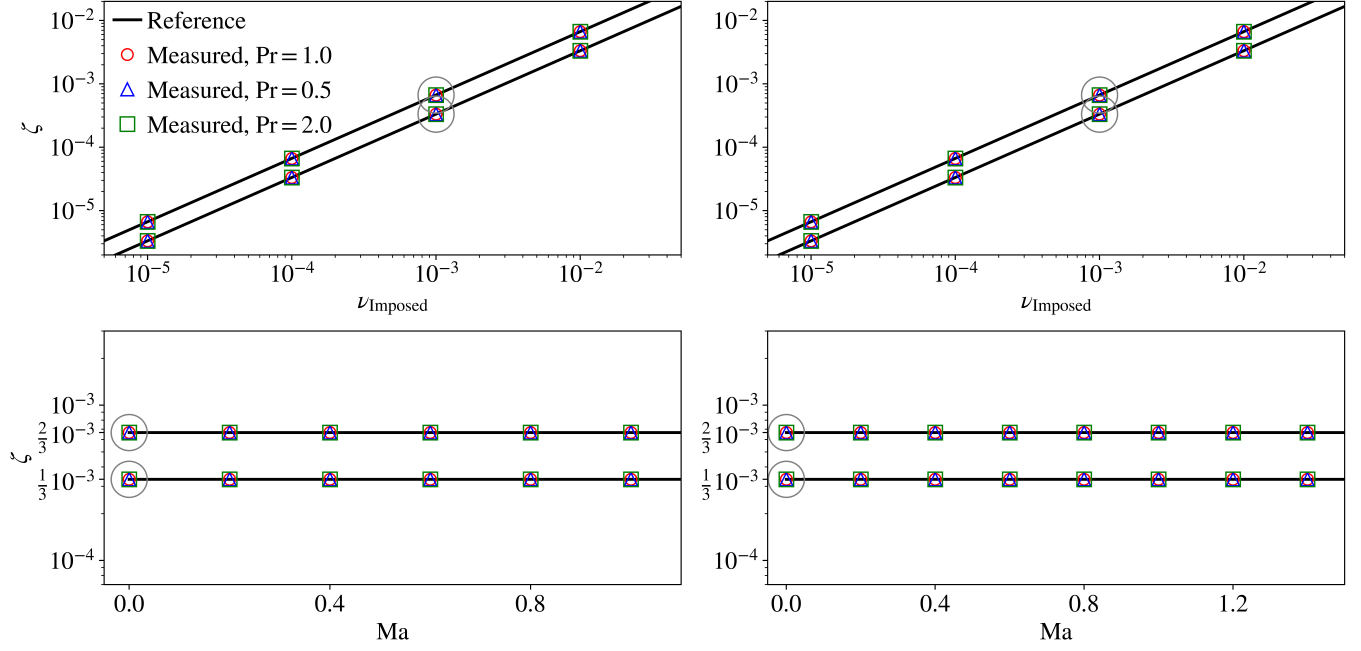


FIG. 5. Results of the dissipation tests for the bulk mode with $\gamma = \{5/3, 8/6\}$ and $\text{Pr} = \{0.5, 1, 2\}$ for the total energy split in the left column and internal-non-translational in the right column. The measured versus imposed values of kinematic bulk viscosity is depicted in the top row at $\text{Ma} = 0$, whereas the bottom row shows the measured values at various Mach numbers. The gray circles indicate corresponding measurement points between the two rows.

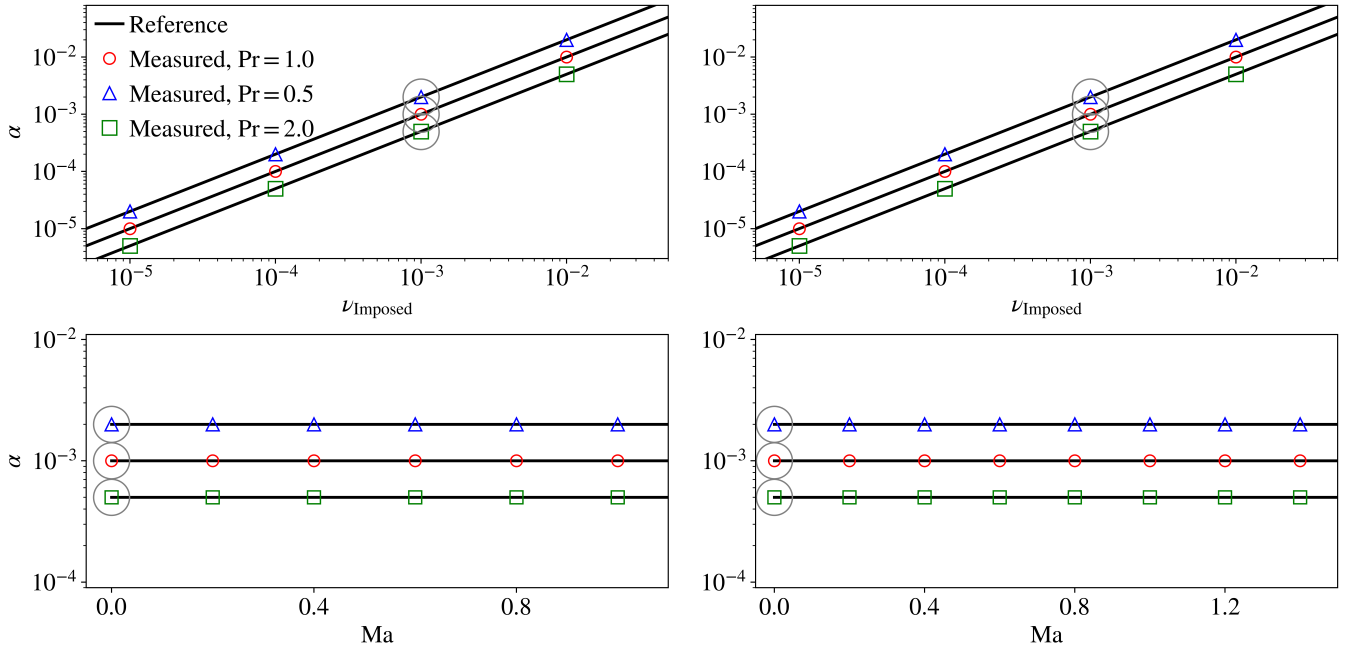


FIG. 6. Results of the dissipation tests for the entropic mode with $\text{Pr} = \{0.5, 1, 2\}$ for the total energy split in the left column and internal-non-translational in the right column. The measured versus imposed values of thermal diffusivity is depicted in the top row at $\text{Ma} = 0$, whereas the bottom row shows the measured values at various Mach numbers. The gray circles indicate corresponding measurement points between the two rows.

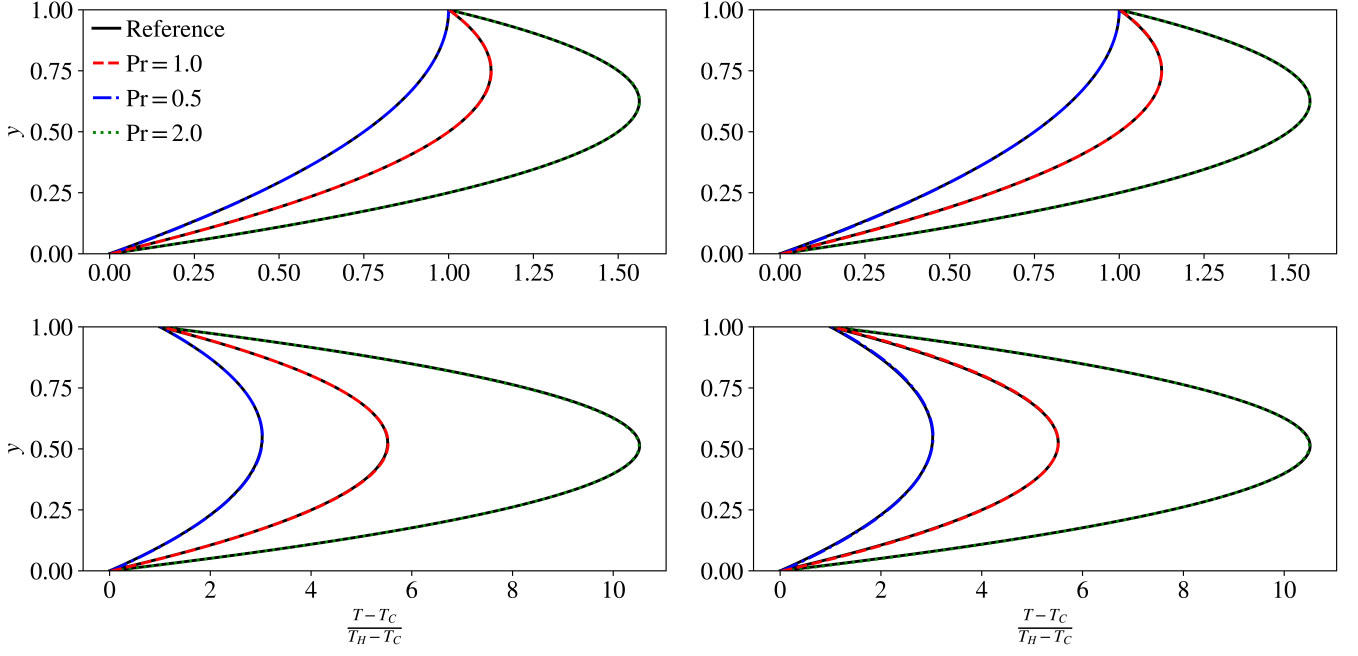


FIG. 7. Results of the thermal Couette problem with $Pr = \{0.5, 1, 2\}$ for the total energy split in the left column and internal-non-translational in the right column. The top row depicts a comparison with the reference solution at $Ma = 0.5$ and $Ec = 4$, whereas the bottom row shows $Ma = 1.2$ and $Ec = 40$.

3. Thermal diffusivity

A different type of perturbation was introduced in the ICs of the system to assess the thermal diffusivity α . These are

$$\rho = \rho_0 + A \sin(2\pi x/L_x), T = \rho_0 T_0 / \rho, u_x = u_0, u_y = 0, \quad (87)$$

with $(\rho_0, T_0) = (1, 1)$ and a perturbation amplitude of $A = 1 \times 10^{-6}$. The thermal diffusivity was measured by fitting the exponential function,

$$T'(t) \propto \exp\left(-\frac{4\pi^2 \alpha}{L_x^2} t\right), \quad (88)$$

to the temporal evolution of the maximum temperature difference $T' = T - T_0$ in the domain.

From Fig. 6 it becomes evident that the models also perform well in terms of thermal dissipation rates, importantly for all the different Prandtl numbers, as the exact expression, cf. Section II C, is accurately recovered.

To summarize the insights from all dissipation tests: All dissipation rates are correctly recovered for a wide range of imposed parameters. The difference in the reported range of Mach numbers is tied to the stability limits associated to the employed velocity sets, and follows the same arguments as in III C. It is known that the D2Q25 which was employed with the internal non-translational energy split, possesses an increased Mach number range as compared to the D2Q16 velocity set, which was employed with the total energy split. These results confirm that the models were correctly constructed for what concerns the Navier–Stokes–Fourier level solutions and dissipation of eigen-modes.

E. Thermal Couette flow

The thermal Couette flow is the next benchmark considered here, to assess the proper recovery of the combined effect of viscous heating and thermal conductivity with the respective Prandtl number. In this test case, an upper no slip wall with the higher temperature $T_W = T_H$ is in motion with a constant speed in x direction $u_{x,W} = u_0$, while the lower no slip wall is at rest, $u_{x,W} = 0$, with a temperature $T_W = T_C$. The parameters for the simulations were set to a Mach number of $Ma = u_0 / \sqrt{\gamma R T_C} = 0.5$ and 1.2 , as well as an Eckert number of $Ec = u_0^2 / (C_p (T_H - T_C)) = 4$ and 40 . Furthermore, the Reynolds number was $Re = \rho u_0 L_y / \mu = 100$, the lower temperature $T_C = T_{ref}$ and the resolution $\delta y = L_y / 128$ in $y \in [0, 1]$. The simulations were initialized with linear temperature pro-

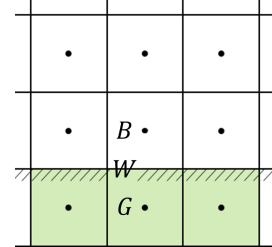


FIG. 8. Schematic of the boundaries for implementation of the boundary conditions.

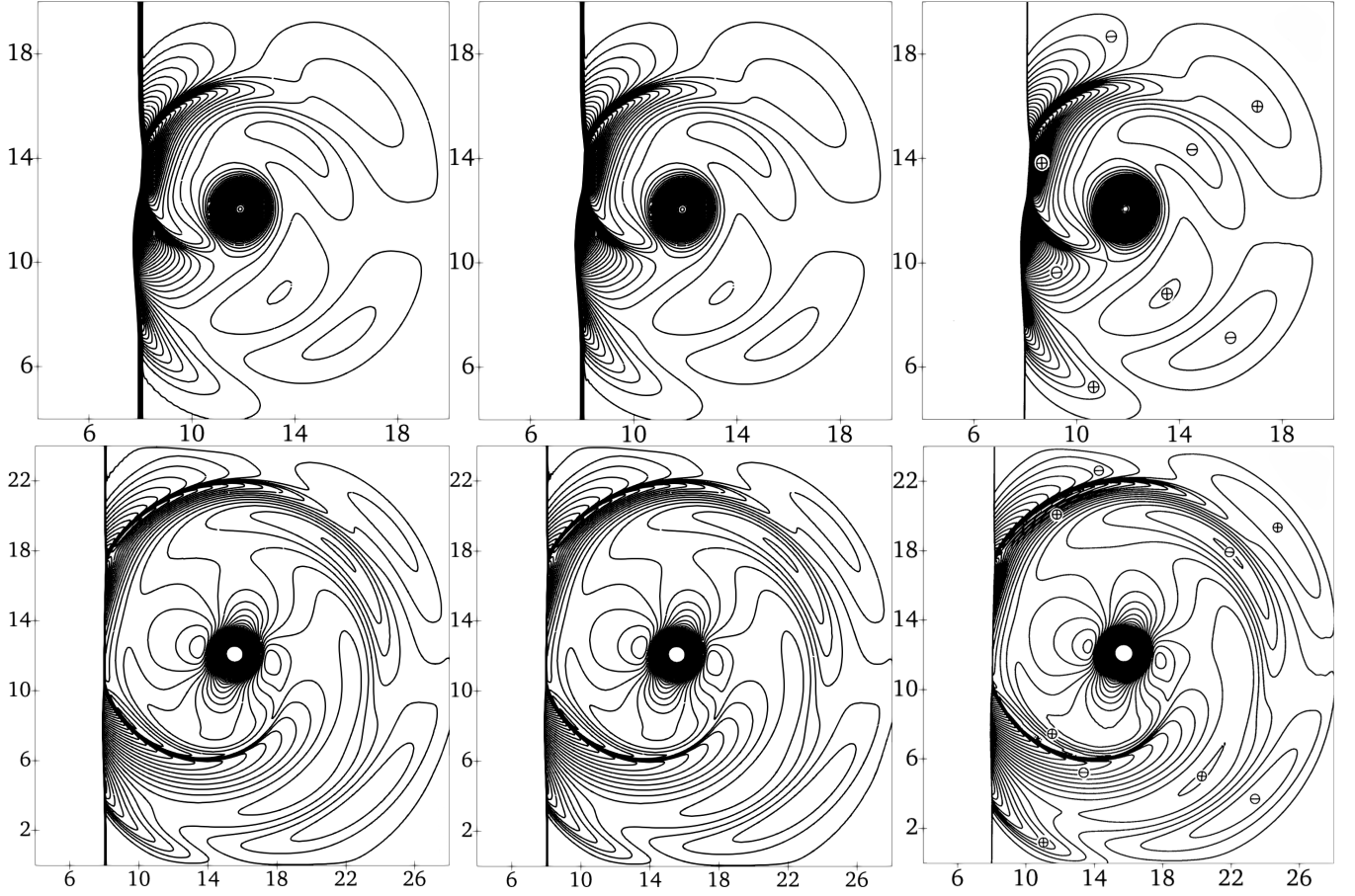


FIG. 9. Results of the shock-vortex interaction. The left and middle column show the model with total and internal-non-translational energy split, whereas Case C ($Ma_s = 1.2$ and $Ma_v = 0.25$) at $t^* = 6$ and case G ($Ma_s = 1.29$ and $Ma_v = 0.39$) at $t^* = 10.3$ are depicted with 140 and 90 equidistant contours of the sound pressure p_{Sound} in the top and bottom row, respectively. The reference solution for both cases C and G from Inoue & Hattori [67] are displayed in the right column.

files in temperature and velocity as

$$(u_x, T, \rho) = (u_0 \frac{y}{L_y}, T_C + (T_H - T_C) \frac{y}{L_y}, \frac{1}{RT_C}), \quad 0 \leq y \leq L_y, \quad (89)$$

and were run until the solution converged.

While periodic BCs were enforced in the horizontal direction, the BC at the no slip walls were implemented via the ghost node approach [46, 68] in combination with non-equilibrium extrapolation approach [47, 69] by splitting the boundary populations into an equilibrium and non-equilibrium part (see also [29, 30, 32] for other valuable approaches in combination with the thermal Couette case). The approach consists of the following steps in accordance with the schematic given in Fig. 8 for the nomenclature. First, the density, flow velocity and temperature are determined in the ghost cell. With the fixed values at the wall and the known values at the boundary nodes, they read

$$\rho_G = \rho_B \quad (90)$$

$$\mathbf{u}_G = 2\mathbf{u}_W - \mathbf{u}_B, \quad (91)$$

$$T_G = 2T_W - T_B. \quad (92)$$

Thereafter, the equilibrium is computed and the non-equilibrium part extrapolated from the neighboring nodes, yielding to the expressions for both f_i and g_i populations as

$$f_i^G = f_i^{\text{eq}}(\rho_G, \mathbf{u}_G, T_G) + f_i^{\text{neq}}(\rho_B, \mathbf{u}_B, T_B) \Big|_G, \quad (93)$$

$$g_i^G = g_i^{\text{eq}}(\rho_G, \mathbf{u}_G, T_G) + g_i^{\text{neq}}(\rho_B, \mathbf{u}_B, T_B) \Big|_G, \quad (94)$$

Fig. 7 depicts the non-dimensional temperature profiles for three different Prandtl numbers at $Ma = 0.5$, $Ec = 4$ and the more pronounced case of $Ma = 1.2$, $Ec = 40$. The analytical solution for the temperature can be written as [70]

$$\frac{T - T_C}{T_H - T_C} = \frac{y}{L_y} + \frac{\text{Pr} \, Ec}{2} \frac{y}{L_y} \left(1 - \frac{y}{L_y}\right). \quad (95)$$

It can clearly be seen that the results are in excellent agreement with the reference solutions.

F. Shock-Vortex interaction

Lastly, a sensitive benchmark problem for viscous compressible flows, namely a shock-vortex interaction, was as-

essed. There, proper recovery of the dissipation rates for non-unity Prandtl numbers together with high resolution is crucial. The setup of Inoue & Hattori [67] as adopted in [39, 50] was followed here, where the main field is separated by a stationary shock with Mach number Ma_s and the left- and right-hand initial states satisfy the Rankine–Hugoniot jump conditions. For a pre-shock state of $(\rho, p, u_x = Ma_s c_s, u_y = 0)_l$ on the left-hand side, where the flow velocity is given from the imposed Ma number via $c_{s,l} = \sqrt{\gamma R T_l} = \sqrt{\gamma p_l / \rho_l}$, the post-shock state $(\rho, p, u_x, u_y = 0)_r$ is found as

$$\rho_r = \rho_l \frac{(\gamma + 1) Ma_s^2}{(\gamma - 1) Ma_s^2 + 2}, \quad (96)$$

$$p_r = p_l \frac{2\gamma Ma_s^2 - (\gamma - 1)}{(\gamma + 1)}, \quad (97)$$

$$u_{x,r} = u_{x,l} \frac{(\gamma - 1) Ma_s^2 + 2}{(\gamma + 1) Ma_s^2}. \quad (98)$$

The resulting initial field $(\rho, p, u_x, u_y)_\infty$ is perturbed by an isentropic vortex which is advected through the shock. The maximum tangential velocity of the vortex defines the vortex Mach number as $Ma_v = u_\phi^{\max} / c_{s,l}$. In Cartesian coordinates, the ICs for the vortex read

$$u_x = u_{x,\infty} + c_{s,l} Ma_v \frac{y - y_v}{r_v} e^{(1-r^2)/2}, \quad (99)$$

$$u_y = u_{y,\infty} - c_{s,l} Ma_v \frac{x - x_v}{r_v} e^{(1-r^2)/2}, \quad (100)$$

$$\rho = \rho_\infty \left[1 - \frac{\gamma - 1}{2} Ma_v^2 e^{(1-r^2)} \right]^{1/(\gamma - 1)}, \quad (101)$$

$$p = p_\infty \left[1 - \frac{\gamma - 1}{2} Ma_v^2 e^{(1-r^2)} \right]^{\gamma/(\gamma - 1)}. \quad (102)$$

Note that the field is perturbed on both sides of the shock to match the reference solution in the DNS setup [67], where the influenced region of the vortex in the IC overlaps the shock slightly. The reduced radius r is defined with the vortex center position (x_v, y_v) and the vortex radius r_v as $r = \sqrt{(x - x_v)^2 + (y - y_v)^2} / r_v$, where the vortex radius is connected to the dynamic viscosity of the fluid via the Reynolds number defined as $Re_v = \rho_l c_{s,l} r_v / \mu$.

The shock position was initialized at $x_s = 8$ with $\rho_l = 1$ and $p_l = 1$ in a domain $x \in [0, 28]$ and $y \in [0, 24]$. The vortex with $r_v = 1$, rotating in clock-wise direction, was centered at $(x_v, y_v) = (6, 12)$. The Reynolds number was set to $Re_v = 800$ and the Prandtl number to $Pr = 0.75$. As in the original setup, periodic BCs were used for the boundaries in y-direction. Cases C and G from [67] were run. For case C, $Ma_s = 1.2$ and $Ma_v = 0.25$ was imposed, whereas for case G, these numbers were set to $Ma_s = 1.29$ and $Ma_v = 0.39$. A resolution of $\delta x = \delta y = L_x / 1680 = L_y / 1440$ was applied.

Fig. 9 depicts the sound pressure contours at the non-dimensional time $t^* = 6$ and $t^* = 10.3$ for case C and G compared to the reference solution. Thereby, the sound pressure is defined as $p_{\text{Sound}} = p / p_r - 1$, with p_r being the initial pressure in the post-shock region, and the non-dimensional time is given by $t^* = t c_{s,l} / r_v$. Note that the sound pressure usually

amounts to a small perturbation in the order of $\lesssim 1\%$ of the hydrodynamic pressure on top of it and is therefore a rather sensitive quantity. Excellent agreement of the pressure contours with the reference DNS solution of [67] can be observed. Importantly, the deformation of the shock, including the two shock reflections, is also well captured.

For further quantitative comparison of case C, the radial distribution of the sound pressure was measured in the direction of $\varphi = 45^\circ$ degrees with the origin at the vortex center.

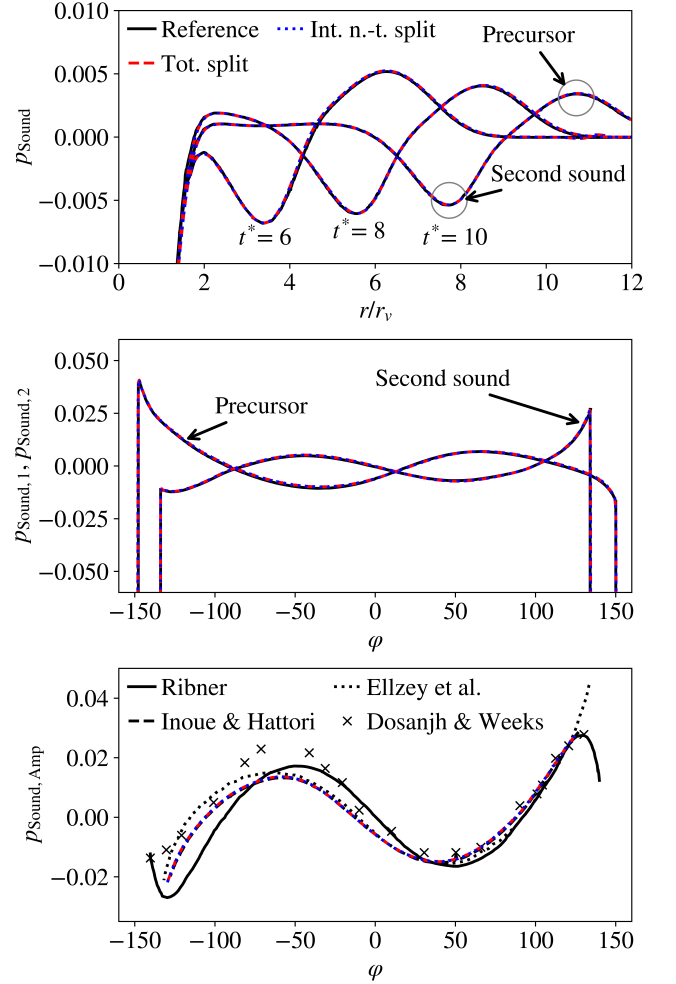


FIG. 10. Quantitative results of the shock-vortex interactions: (Top) Comparison of the radial sound pressure distribution of case C ($Ma_s = 1.2$ and $Ma_v = 0.25$) at three different non-dimensional times $t^* = 6, 8, 10$ with the reference solution from Inoue & Hattori [67]. The gray circles indicate the peak sound pressure of the precursor, $p_{\text{Sound},1}$, and the second sound, $p_{\text{Sound},2}$. (Middle) Comparison of the circumferential distribution of the peak sound pressure of the precursor, $p_{\text{Sound},1}$, and the second sound, $p_{\text{Sound},2}$, for case G ($Ma_s = 1.29$ and $Ma_v = 0.39$) at non-dimensional time $t^* = 10.3$ with the reference solution from Inoue & Hattori [67]. (Bottom) Comparison of the circumferential distribution of the sound pressure amplitude, $p_{\text{Sound,amp}}$, of case G ($Ma_s = 1.29$ and $Ma_v = 0.39$) with theoretical results of Ribner [71], viscous DNS simulations of Inoue & Hattori [67], inviscid simulations by Ellzey et al. [72], and experimental results by Dosanjh & Weeks [73].

The results are depicted in Fig. 10 (top) for three different non-dimensional times t^* . It can clearly be seen that the reference solutions are perfectly matched. In particular, the temporal development of the position and magnitude of the peak sound pressure of the first sound (precursor) and the second sound emerging from the shock-vortex interaction are well captured.

For quantitative comparison of case G, the sound pressure amplitude $p_{\text{Sound,amp}}$ is compared to inviscid and viscous DNS simulations, experimental results as well as theory. Thereby, the sound pressure amplitude is computed as $p_{\text{Sound,Amp}} = (p_2 - p_1)/p_r$, i.e. the difference between the peak sound pressure of the precursor, denoted as $p_{\text{Sound,1}} = p_1/p_r - 1$, and the second sound, $p_{\text{Sound,2}} = p_2/p_r - 1$, where p_1 and p_2 are measured equivalently to [67] at $r/r_v = 10.8$ and $r/r_v = 8.8$ from the vortex center, respectively. The results for the circumferential distribution of $p_{\text{Sound,1}}$ and $p_{\text{Sound,2}}$ are depicted against the reference solutions [67] as an intermediate result in Fig. 10 (middle), and the results for the circumferential distribution of $p_{\text{Sound,Amp}}$ are shown in Fig. 10 (bottom). It can be seen that the reference solution of the viscous simulation [67] is perfectly matched for both models for non-unity Prandtl number with the total versus internal non-translational energy split, respectively. The results lie well within the knowledge band acquired by former viscous and inviscid simulations [67, 72], experimental measurements [73] conducted at a much higher Reynolds number of $\text{Re} \approx 1.6 \times 10^5$, and theoretical results [71].

These insights further validate the presented models and demonstrate an excellent performance in obtaining sensitive quantities at the Navier–Stokes–Fourier level for complex setups in compressible and moderately supersonic flows with variable Prandtl numbers.

IV. SUMMARY, CONCLUSIONS AND OUTLOOK

In this work, a consistent kinetic modeling and discretization approach for compressible flow simulation across arbitrary Prandtl numbers and specific heat ratios is discussed. Using the quasi-equilibrium method within two double-distribution function approaches, the models recover full Navier–Stokes–Fourier dynamics, including all correct macroscopic moments and dissipation rates. The construction of the quasi-equilibria is demonstrated through rigorous hydrodynamic analysis. Higher-order static velocity sets in the context of a discrete velocity Boltzmann method enable an accurate discrete representation without the necessity for correction terms.

The models were validated against sensitive benchmarks, demonstrating physical fidelity, strict conservation, stability, and Galilean invariance across demanding flow conditions. Correct dispersion and dissipation behavior was recovered across a temperature range covering orders of magnitude and a broad range of Mach numbers. Due to the application of the D2Q16 velocity set, the total energy split exhibited a superior temperature range over the internal non-translational split, which performed over a wider Mach number range due to the requirement of employing the D2Q25. Lastly, a suc-

cessful and very accurate reproduction of the solutions of a thermal Couette flow and a viscous shock–vortex interaction confirmed the models’ practical viability. These insights showcase that the presented models offer an efficient and scalable framework for simulating compressible fluid dynamics with variable Prandtl numbers, while ensuring thermodynamic consistency, strict conservation of key physical quantities, and accurate reproduction of Navier–Stokes–Fourier-level behavior.

Although restricted to higher-order lattices in this manuscript, future work shall also focus on the application of correction terms to accommodate standard lattices for usage with the lattice Boltzmann method, such as in [50], as well as the extension with shifted, scaled, and adaptive reference frames, such as in the particles on demand method [43], in order to simulate high-Mach, strong discontinuities and hypersonic regimes. Furthermore, application of space-time adaptive conservative refinement methods, such as in [39], marks a promising avenue to increase computational efficiency.

ACKNOWLEDGMENTS

This work was supported by the European Research Council (ERC) Advanced Grant No. 834763-PonD and by the Swiss National Science Foundation (SNSF) Grant Nos. 200021-228065 and 200021-236715. Computational resources at the Swiss National Super Computing Center (CSCS) were provided under Grant Nos. s1286, sm101 and s1327. Open access funding was provided by the Swiss Federal Institute of Technology Zürich (ETH Zürich).

AUTHOR DECLARATIONS

Conflict of interest

The authors have no conflicts to disclose.

Ethical approval

The work presented here by the authors did not require ethics approval or consent to participate.

Author contributions

R.M.S.: Conceptualization of the study, formal analysis, derivation and development of the methodology, implementation of the solver, evaluation and data analysis, writing- initial manuscript and revised versions. S.A.H.: Conceptualization of the study, writing- initial manuscript and revised versions. I.V.K.: Conceptualization of the study, writing- initial manuscript and revised versions, funding acquisition, resources. All authors approved the final manuscript.

Data availability statement

The data that support the findings of this study are available within the article or from the corresponding author(s) upon reasonable request.

Open access

This article is licensed under a Creative Commons Attribution 4.0 International License, which permits use, sharing, adaptation, distribution and reproduction in any medium or format, as long as you give appropriate credit to the original author(s)

and the source, provide a link to the Creative Commons license, and indicate if changes were made. The images or other third party material in this article are included in the article's Creative Commons license, unless indicated otherwise in a credit line to the material. If material is not included in the article's Creative Commons license and your intended use is not permitted by statutory regulation or exceeds the permitted use, you will need to obtain permission directly from the copyright holder. To view a copy of this license, visit <http://creativecommons.org/licenses/by/4.0/>.

Appendix A: Relevant equilibrium and conserved moments

The moments of the Maxwell–Boltzmann distribution relevant to the models outlined in this manuscript are found as follows, denoted in index notation with summation convention. The conserved moments read

$$\int \{f^{\text{eq}}, f, f^*\} d\mathbf{v} = \rho, \quad (\text{A1})$$

$$\int v_\alpha \{f^{\text{eq}}, f, f^*\} d\mathbf{v} = \rho u_\alpha, \quad (\text{A2})$$

$$\left. \begin{aligned} \text{(I)} \quad & \int \{g^{\text{eq}}, g, g^*\} d\mathbf{v} \\ \text{(II)} \quad & \int \{g^{\text{eq}}, g, g^*\} + \frac{v^2}{2} \{f^{\text{eq}}, f^*, f\} d\mathbf{v} \end{aligned} \right\} = \rho \left(C_v T + \frac{u_\gamma u_\gamma}{2} \right) = E, \quad (\text{A3})$$

the higher-order moments of the f^{eq} -distribution read,

$$\int v_\alpha v_\beta f^{\text{eq}} d\mathbf{v} = \rho u_\alpha u_\beta + \rho RT \delta_{\alpha\beta}, \quad (\text{A4})$$

$$\int v_\alpha v_\beta v_\gamma f^{\text{eq}} d\mathbf{v} = \rho u_\alpha u_\beta u_\gamma + \rho RT [u_\alpha \delta_{\beta\gamma}]_{\text{cyc}}, \quad (\text{A5})$$

$$\int v_\alpha v_\beta v_\gamma v_\delta f^{\text{eq}} d\mathbf{v} = \rho u_\alpha u_\beta u_\gamma u_\delta + \rho RT [u_\alpha u_\beta \delta_{\gamma\delta}]_{\text{cyc}} + \rho (RT)^2 [\delta_{\alpha\beta} \delta_{\gamma\delta}]_{\text{cyc}}, \quad (\text{A6})$$

and the higher-order moments involving the g^{eq} -distribution read,

$$\left. \begin{aligned} \text{(I)} \quad & \int v_\alpha g^{\text{eq}} d\mathbf{v} \\ \text{(II)} \quad & \int v_\alpha g^{\text{eq}} + v_\alpha \frac{v^2}{2} f^{\text{eq}} d\mathbf{v} \end{aligned} \right\} = u_\alpha (E + \rho RT), \quad (\text{A7})$$

$$\left. \begin{aligned} \text{(I)} \quad & \int v_\alpha v_\beta g^{\text{eq}} d\mathbf{v} \\ \text{(II)} \quad & \int v_\alpha v_\beta g^{\text{eq}} + v_\alpha v_\beta \frac{v^2}{2} f^{\text{eq}} d\mathbf{v} \end{aligned} \right\} = \rho RT u_\alpha u_\beta + (E + \rho RT)(u_\alpha u_\beta + RT \delta_{\alpha\beta}). \quad (\text{A8})$$

Furthermore, by substitution of the contracted higher-order moments of f^{eq} (divided by two), i.e.

$$\int \frac{v^2}{2} f^{\text{eq}} d\mathbf{v} = \rho \frac{u^2}{2} + \rho RT \frac{D}{2}, \quad (\text{A9})$$

$$\int v_\alpha \frac{v^2}{2} f^{\text{eq}} d\mathbf{v} = \rho u_\alpha \frac{u^2}{2} + \rho RT \frac{u_\alpha (D+2)}{2}, \quad (\text{A10})$$

$$\int v_\alpha v_\beta \frac{v^2}{2} f^{\text{eq}} d\mathbf{v} = \rho u_\alpha u_\beta \frac{u^2}{2} + \rho RT \frac{u_\alpha u_\beta (D+4) + u^2 \delta_{\alpha\beta}}{2} + \rho (RT)^2 \frac{\delta_{\alpha\beta} (D+2)}{2}, \quad (\text{A11})$$

into Eqs. (A3), (A7) and (A8), one obtains the following equilibrium moments of g for the internal non-translational energy split,

$$\text{(II)} \quad \int g^{\text{eq}} d\mathbf{v} = E - \left(\rho \frac{u^2}{2} + \rho RT \frac{D}{2} \right) = \rho \left(C_v T - RT \frac{D}{2} \right), \quad (\text{A12})$$

$$\text{(II)} \quad \int v_\alpha g^{\text{eq}} d\mathbf{v} = u_\alpha (E + \rho RT) - \left(\rho u_\alpha \frac{u^2}{2} + \rho RT \frac{u_\alpha (D+2)}{2} \right) = \rho \left(C_v T - RT \frac{D}{2} \right) u_\alpha, \quad (\text{A13})$$

$$\begin{aligned} \text{(II)} \quad \int v_\alpha v_\beta g^{\text{eq}} d\mathbf{v} &= \rho RT u_\alpha u_\beta + (E + \rho RT)(u_\alpha u_\beta + RT \delta_{\alpha\beta}) \\ &\quad - \left(\rho u_\alpha u_\beta \frac{u^2}{2} + \rho RT \frac{u_\alpha u_\beta (D+4) + u^2 \delta_{\alpha\beta}}{2} \right. \\ &\quad \left. + \rho (RT)^2 \frac{\delta_{\alpha\beta} (D+2)}{2} \right) \\ &= \rho \left(C_v T - RT \frac{D}{2} \right) (u_\alpha u_\beta + RT \delta_{\alpha\beta}). \end{aligned} \quad (\text{A14})$$

Note that a moment of the Maxwell–Boltzmann distribution can also be computed from the next lower order moment by application of the operator

$$\mathcal{O}_\alpha A = RT \partial_{u_\alpha} A + u_\alpha A. \quad (\text{A15})$$

Hence, all Maxwell–Boltzmann energy moments can be written as the result of repeated application of operators on the generating function, i.e. Eq. (33).

Appendix B: Hydrodynamic limit

A multiscale analysis in the form of the Chapman-Enskog expansion [7] is conducted hereafter. The starting point is the following system of equations,

$$\begin{aligned} \partial_t \{f, g\} + \mathbf{v} \cdot \nabla \{f, g\} &= -\frac{1}{\tau_1} (\{f, g\} - \{f^*, g^*\}) \\ &\quad - \frac{1}{\tau_2} (\{f^*, g^*\} - \{f^{\text{eq}}, g^{\text{eq}}\}), \end{aligned} \quad (\text{B1})$$

where the following parameters are introduced:

- Characteristic flow velocity \mathcal{U} ,
- Characteristic flow scale \mathcal{L} ,
- Characteristic flow time $\mathcal{T} = \mathcal{L}/\mathcal{U}$,
- Characteristic density $\bar{\rho}$,
- Speed of sound of an ideal gas $c_s = \sqrt{\gamma RT}$.

With these, the variables are reduced as follows (primes denote non-dimensional variables):

- Time $t = \mathcal{T}t'$,
- Space $\mathbf{r} = \mathcal{L}\mathbf{r}'$,
- Flow velocity $\mathbf{u} = \mathcal{U}\mathbf{u}'$,
- Particle velocity $\mathbf{v} = c_s\mathbf{v}'$,
- Density $\rho = \bar{\rho}\rho'$,
- Distribution function $f = \bar{\rho}c_s^{-3}f'$.

Furthermore, the following non-dimensional groups are introduced:

- Knudsen number, $\text{Kn} = \tau c_s/\mathcal{L}$,
- Mach number, $\text{Ma} = \mathcal{U}/c_s$.

With these, the equations are rescaled as

$$\begin{aligned} \text{Ma Kn} (\partial_t' \{f', g'\} + \mathbf{v}' \cdot \nabla' \{f', g'\}) = \\ - \frac{1}{\tau_1'} (\{f', g'\} - \{f^{*'}, g^{*'}\}) \\ - \frac{1}{\tau_2'} (\{f^{*'}, g^{*'}\} - \{f^{\text{eq}'}, g^{\text{eq}'}\}). \end{aligned} \quad (\text{B2})$$

Of interest here is $\text{Ma} \sim 1$, $\text{Kn} \sim \varepsilon$, i.e. the hydrodynamic limit. After dropping the primes for the sake of readability,

$$\begin{aligned} \varepsilon (\partial_t \{f, g\} + \mathbf{v} \cdot \nabla \{f, g\}) = - \frac{1}{\tau_1} (\{f, g\} - \{f^*, g^*\}) \\ - \frac{1}{\tau_2} (\{f^*, g^*\} - \{f^{\text{eq}}, g^{\text{eq}}\}). \end{aligned} \quad (\text{B3})$$

and introducing the multiscale expansions in the distribution functions,

$$\begin{aligned} \{f, g, f^*, g^*\} = \{f^{(0)}, g^{(0)}, f^{*(0)}, g^{*(0)}\} \\ + \varepsilon \{f^{(1)}, g^{(1)}, f^{*(1)}, g^{*(1)}\} \\ + \varepsilon^2 \{f^{(2)}, g^{(2)}, f^{*(2)}, g^{*(2)}\} + O(\varepsilon^3), \end{aligned} \quad (\text{B4})$$

as well as the time derivative operator,

$$\partial_t = \partial_t^{(1)} + \varepsilon \partial_t^{(2)} + O(\varepsilon^2), \quad (\text{B5})$$

the following equations are recovered at scales ε^0 , ε^1 and ε^2 :

$$\begin{aligned} \varepsilon^0 : 0 = - \frac{1}{\tau_1} (\{f^{(0)}, g^{(0)}\} - \{f^{*(0)}, g^{*(0)}\}) \\ - \frac{1}{\tau_2} (\{f^{*(0)}, g^{*(0)}\} - \{f^{\text{eq}}, g^{\text{eq}}\}), \end{aligned} \quad (\text{B6})$$

$$\begin{aligned} \varepsilon^1 : \partial_t^{(1)} \{f^{(0)}, g^{(0)}\} + \mathbf{v} \cdot \nabla \{f^{(0)}, g^{(0)}\} = \\ - \frac{1}{\tau_1} \{f^{(1)}, g^{(1)}\} + \left(\frac{1}{\tau_1} - \frac{1}{\tau_2} \right) \{f^{*(1)}, g^{*(1)}\}, \end{aligned} \quad (\text{B7})$$

$$\begin{aligned} \varepsilon^2 : \partial_t^{(1)} \{f^{(1)}, g^{(1)}\} + \mathbf{v} \cdot \nabla \{f^{(1)}, g^{(1)}\} + \partial_t^{(2)} \{f^{(0)}, g^{(0)}\} = \\ - \frac{1}{\tau_1} \{f^{(2)}, g^{(2)}\} + \left(\frac{1}{\tau_1} - \frac{1}{\tau_2} \right) \{f^{*(2)}, g^{*(2)}\}. \end{aligned} \quad (\text{B8})$$

Note that for the sake of readability, writing the factors $\{\varepsilon^0, \varepsilon^1, \varepsilon^2\}$ in front of every term was omitted for the remainder of the analysis. However it shall be kept in mind that, e.g. the whole order-2-in- ε equation would possess a prefactor of ε^2 . An analysis on each order-in- ε equation will follow.

From order ε^0 it directly follows that

$$\{f^{(0)}, g^{(0)}\} = \{f^{*(0)}, g^{*(0)}\} = \{f^{\text{eq}}, g^{\text{eq}}\}, \quad (\text{B9})$$

for any τ_1, τ_2 . Note that, therefore, the solvability conditions for this system for $\forall k > 0$, which can be inferred from the equations provided in Section II B, become

$$\int \{f^{(k)}, f^{*(k)}\} d\mathbf{v} = 0, \quad (\text{B10})$$

$$\int \mathbf{v} \{f^{(k)}, f^{*(k)}\} d\mathbf{v} = 0, \quad (\text{B11})$$

$$\text{(I)} \quad \int \{g^{(k)}, g^{*(k)}\} d\mathbf{v} = 0,$$

$$\text{(II)} \quad \int \{g^{(k)}, g^{*(k)}\} + \frac{v^2}{2} \{f^{(k)}, f^{*(k)}\} d\mathbf{v} = 0, \quad (\text{B12})$$

for the conserved moments. Further solvability conditions related to Prandtl numbers $\{\text{Pr} \leq 1, \text{Pr} \geq 1\}$ for $\forall k > 0$ read

$$\int \mathbf{v} \otimes \mathbf{v} f^{*(k)} d\mathbf{v} = 0, \quad (\text{B13})$$

$$\begin{aligned} \text{(I)} \quad \int \mathbf{v} g^{*(k)} d\mathbf{v} - \mathbf{u} \cdot \int \mathbf{v} \otimes \mathbf{v} f^{*(k)} d\mathbf{v} \\ = \int \mathbf{v} g^{(k)} d\mathbf{v} - \mathbf{u} \cdot \int \mathbf{v} \otimes \mathbf{v} f^{(k)} d\mathbf{v}, \\ \text{(II)} \quad \int \mathbf{v} g^{*(k)} + \mathbf{v} \frac{v^2}{2} f^{*(k)} d\mathbf{v} - \mathbf{u} \cdot \int \mathbf{v} \otimes \mathbf{v} f^{*(k)} d\mathbf{v} \\ = \int \mathbf{v} g^{(k)} + \mathbf{v} \frac{v^2}{2} f^{(k)} d\mathbf{v} - \mathbf{u} \cdot \int \mathbf{v} \otimes \mathbf{v} f^{(k)} d\mathbf{v}, \end{aligned} \quad (\text{B14})$$

for $\text{Pr} \leq 1$, i.e. in case the quasi-equilibria are constructed using minimization under constraints of conserving mass, momentum, total energy, and the pressure tensor, while the heat flux vector is quasi-conserved. For the opposite case where the quasi-equilibria are constructed under constraints of conserving mass, momentum, total energy, and the heat flux vector, while the pressure tensor is quasi-conserved, i.e. for $\text{Pr} \geq 1$, the solvability conditions read

$$\int \mathbf{v} \otimes \mathbf{v} f^{*(k)} d\mathbf{v} = \int \mathbf{v} \otimes \mathbf{v} f^{(k)} d\mathbf{v}, \quad (\text{B15})$$

$$\text{(I)} \quad \int \mathbf{v} g^{*(k)} d\mathbf{v} - \mathbf{u} \cdot \int \mathbf{v} \otimes \mathbf{v} f^{*(k)} d\mathbf{v} = 0,$$

$$\text{(II)} \quad \int \mathbf{v} g^{*(k)} + \mathbf{v} \frac{v^2}{2} f^{*(k)} d\mathbf{v} - \mathbf{u} \cdot \int \mathbf{v} \otimes \mathbf{v} f^{*(k)} d\mathbf{v} = 0. \quad (\text{B16})$$

Next, going up one order in ε and computing the moments $\int \{f, \mathbf{v}f\} d\mathbf{v}$ of the Chapman–Enskog-expanded equations at order ε , using the solvability conditions and the known equilibrium moments (listed in Appendix A), the continuity and momentum balance equations become

$$\partial_t^{(1)} \rho + \nabla \cdot \rho \mathbf{u} = 0, \quad (\text{B17})$$

$$\partial_t^{(1)} (\rho \mathbf{u}) + \nabla \cdot (\rho \mathbf{u} \otimes \mathbf{u} + p \mathbf{I}) = 0, \quad (\text{B18})$$

written in vector notation with the identity tensor \mathbf{I} . For the energy balance equation, computing the moment $\{(\text{I}) \int g d\mathbf{v}, (\text{II}) \int g + \frac{v^2}{2} f d\mathbf{v}\}$ results in

$$\partial_t^{(1)} E + \nabla \cdot (E + p) \mathbf{u} = 0, \quad (\text{B19})$$

for both energy splits. Note that a truncation of the expansion at this level, i.e. ε times Eq. $\{(\text{B17}), (\text{B18}), (\text{B19})\}$, yields the compressible Euler equations as

$$\partial_t \rho + \nabla \cdot \rho \mathbf{u} = 0, \quad (\text{B20})$$

$$\partial_t (\rho \mathbf{u}) + \nabla \cdot (\rho \mathbf{u} \otimes \mathbf{u} + p \mathbf{I}) = 0, \quad (\text{B21})$$

$$\partial_t E + \nabla \cdot (E + p) \mathbf{u} = 0, \quad (\text{B22})$$

after using Eq. (B5) truncated at $\partial_t = \partial_t^{(1)} + \mathcal{O}(\varepsilon)$ and transforming back to dimensional variables.

Further transport equations for p , $\rho \mathbf{u}$ and $E \mathbf{u}$, which are relevant for the remainder of the multiscale analysis at order ε^2 , may also be derived at this stage. A transport equation for p is obtained via the balance equations for kinetic and internal energy. A balance equation for kinetic energy can be derived by multiplying the Euler level momentum balance, i.e. Eq. (B18), with \mathbf{u} , as

$$\mathbf{u} \cdot [\partial_t (\rho \mathbf{u}) + \nabla \cdot (\rho \mathbf{u} \otimes \mathbf{u} + p \mathbf{I})] = \mathbf{u} \cdot \partial_t (\rho \mathbf{u}) + \mathbf{u} \cdot (\nabla \cdot \rho \mathbf{u} \otimes \mathbf{u}) + \mathbf{u} \cdot \nabla p = 0. \quad (\text{B23})$$

Using the expansions

$$\mathbf{u} \cdot \partial_t^{(1)} (\rho \mathbf{u}) = \partial_t^{(1)} \left(\underbrace{\frac{1}{2} \rho u^2}_K \right) + \frac{1}{2} u^2 \overbrace{\partial_t^{(1)} \rho}^{-\nabla \cdot \rho \mathbf{u}}, \quad (\text{B24})$$

$$\mathbf{u} \cdot (\nabla \cdot \rho \mathbf{u} \otimes \mathbf{u}) = \nabla \cdot \left(\underbrace{\frac{1}{2} \rho u^2 \mathbf{u}}_{K \mathbf{u}} \right) + \frac{1}{2} u^2 \nabla \cdot \rho \mathbf{u}, \quad (\text{B25})$$

where the time derivative is replaced in favor of a spatial derivative by means of the Euler level continuity, i.e. (B17), results in

$$\partial_t^{(1)} K + \nabla \cdot K \mathbf{u} + \mathbf{u} \cdot \nabla p = 0. \quad (\text{B26})$$

In turn, this can be used to derive a balance equation for internal energy by subtraction from the balance equation for total energy, i.e. Eq.(B19), as

$$\partial_t^{(1)} E - \partial_t^{(1)} K + \nabla \cdot E \mathbf{u} - \nabla \cdot K \mathbf{u} + \nabla \cdot p \mathbf{u} - \mathbf{u} \cdot \nabla p = 0. \quad (\text{B27})$$

By applying the expansion

$$\nabla \cdot p \mathbf{u} - \mathbf{u} \cdot \nabla p = p \nabla \cdot \mathbf{u}, \quad (\text{B28})$$

this results in

$$\partial_t^{(1)} U + \nabla \cdot U \mathbf{u} + p \nabla \cdot \mathbf{u} = 0, \quad (\text{B29})$$

from which a balance equation for pressure can be derived using $\partial_t U = \rho C_v$ together with the ideal gas equation of state as

$$\partial_p U = C_v / R, \quad (\text{B30})$$

resulting in

$$\partial_t^{(1)} p + \nabla \cdot p \mathbf{u} + \frac{R}{C_v} p \nabla \cdot \mathbf{u} = 0. \quad (\text{B31})$$

Furthermore, for the purpose of deriving a transport equation for $\rho \mathbf{u}$, Eq. (B31) is multiplied by \mathbf{u} , as

$$\mathbf{u} \left[\partial_t^{(1)} p + \nabla \cdot p \mathbf{u} + \frac{R}{C_v} p \nabla \cdot \mathbf{u} \right] + \mathbf{u} \partial_t^{(1)} p + \mathbf{u} (\nabla \cdot p \mathbf{u}) + \frac{R}{C_v} p \mathbf{u} (\nabla \cdot \mathbf{u}) = 0. \quad (\text{B32})$$

Using Euler level momentum balance, i.e. (B18), expanded as

$$\begin{aligned} \partial_t^{(1)} (\mathbf{u}) &= -\frac{1}{\rho} \left(\underbrace{\mathbf{u} \partial_t^{(1)} \rho}_{-\nabla \cdot \rho \mathbf{u}} + \underbrace{\rho \mathbf{u} \nabla \cdot \mathbf{u} + (\nabla \cdot \rho \mathbf{u}) \mathbf{u}}_{\nabla \cdot \rho \mathbf{u} \otimes \mathbf{u}} + \nabla p \right) \\ &= -\mathbf{u} \cdot \nabla \mathbf{u} - \frac{1}{\rho} \nabla p, \end{aligned} \quad (\text{B33})$$

the first term can be expanded as

$$\begin{aligned} \mathbf{u} \partial_t^{(1)} p &= \partial_t^{(1)} (p \mathbf{u}) - p \partial_t^{(1)} \mathbf{u} \\ &= \partial_t^{(1)} (p \mathbf{u}) + p \mathbf{u} \cdot \nabla \mathbf{u} + \frac{p}{\rho} \nabla p, \end{aligned} \quad (\text{B34})$$

whereas the second term can be rewritten as

$$\mathbf{u} (\nabla \cdot p \mathbf{u}) = \nabla \cdot p \mathbf{u} \otimes \mathbf{u} - p \mathbf{u} \cdot \nabla \mathbf{u}, \quad (\text{B35})$$

resulting in

$$\partial_t^{(1)} p \mathbf{u} + \nabla \cdot p \mathbf{u} \otimes \mathbf{u} + \frac{p}{\rho} \nabla p + \frac{R}{C_v} p \mathbf{u} \nabla \cdot \mathbf{u} = 0. \quad (\text{B36})$$

Using the same approach to derive a balance equation for $E \mathbf{u}$, starting off with Eq. (B19), multiplying by \mathbf{u} as

$$\begin{aligned} \mathbf{u} \left[\partial_t^{(1)} E + \nabla \cdot E \mathbf{u} + \nabla \cdot p \mathbf{u} \right] + \mathbf{u} \partial_t^{(1)} E + \mathbf{u} (\nabla \cdot E \mathbf{u}) + \mathbf{u} (\nabla \cdot p \mathbf{u}) &= 0, \end{aligned} \quad (\text{B37})$$

using the expansions

$$\begin{aligned} \mathbf{u} \partial_t^{(1)} E &= \partial_t^{(1)} (E \mathbf{u}) - E \partial_t^{(1)} (\mathbf{u}) \\ &= \partial_t^{(1)} (E \mathbf{u}) + E \mathbf{u} \cdot \nabla \mathbf{u} + \frac{E}{\rho} \nabla p, \end{aligned} \quad (\text{B38})$$

$$\mathbf{u} (\nabla \cdot E \mathbf{u}) = \nabla \cdot E \mathbf{u} \otimes \mathbf{u} - E \mathbf{u} \cdot \nabla \mathbf{u}, \quad (\text{B39})$$

and Eq. (B35), the following additional balance equation is received as

$$\partial_t^{(1)} E \mathbf{u} + \nabla \cdot (E + p) \mathbf{u} \otimes \mathbf{u} + \frac{E}{\rho} \nabla p - p \mathbf{u} \cdot \nabla \mathbf{u} = 0. \quad (\text{B40})$$

Next, going up one more order in ε and computing the moments $\int \{f, \mathbf{v}f\} d\mathbf{v}$ of the Chapman–Enskog-expanded equations at order ε^2 , the continuity equation becomes

$$\partial_t^{(2)} \rho = 0, \quad (\text{B41})$$

while for the momentum balance equation one has

$$\partial_t^{(2)} (\rho \mathbf{u}) + \nabla \cdot \int \mathbf{v} \otimes \mathbf{v} f^{(1)} d\mathbf{v} = 0. \quad (\text{B42})$$

The second term can be further expanded using the moment $\int \mathbf{v} \otimes \mathbf{v} f d\mathbf{v}$ of the first-order-in- ε equation, rearranged as

$$\begin{aligned} -\frac{1}{\tau_1} \int \mathbf{v} \otimes \mathbf{v} f^{(1)} d\mathbf{v} + \left(\frac{1}{\tau_1} - \frac{1}{\tau_2} \right) \int \mathbf{v} \otimes \mathbf{v} f^{*(1)} d\mathbf{v} = \\ \partial_t^{(1)} \int \mathbf{v} \otimes \mathbf{v} f^{(0)} d\mathbf{v} + \nabla \cdot \int \mathbf{v} \otimes \mathbf{v} \otimes \mathbf{v} f^{(0)} d\mathbf{v}. \end{aligned} \quad (\text{B43})$$

Here, the expansion depends on the construction of the quasi-equilibria attractors depending on the case of $\{\text{Pr} \leq 1, \text{Pr} \geq 1\}$. After plugging the equilibrium moments into the terms on the RHS and applying the solvability conditions for the QE term on the LHS, one gets

$$\begin{aligned} \int \mathbf{v} \otimes \mathbf{v} f^{(1)} d\mathbf{v} = -\{\tau_1, \tau_2\} \left[\partial_t^{(1)} (\rho \mathbf{u} \otimes \mathbf{u} + p \mathbf{I}) \right. \\ \left. + \nabla \cdot \rho \mathbf{u} \otimes \mathbf{u} + \nabla p \mathbf{u} + (\nabla p \mathbf{u})^\dagger + \mathbf{I} \nabla \cdot p \mathbf{u} \right]. \end{aligned} \quad (\text{B44})$$

Note that, in the prefactor $\{\tau_1, \tau_2\}$, the τ_1 emerges after application of solvability condition (B13), whereas τ_2 emerges after application of solvability condition (B15). Expanding the term

$$\begin{aligned} \partial_t^{(1)} (\rho \mathbf{u} \otimes \mathbf{u} + p \mathbf{I}) = \mathbf{u} \otimes \partial_t^{(1)} \rho \mathbf{u} + (\mathbf{u} \otimes \partial_t^{(1)} \rho \mathbf{u})^\dagger \\ - \mathbf{u} \otimes \mathbf{u} \partial_t^{(1)} \rho + \partial_t^{(1)} p \mathbf{I}, \end{aligned} \quad (\text{B45})$$

and replacing the time derivatives in favor of a spatial derivatives by means of the Euler level continuity, momentum and pressure balance equations, i.e. Eqs. (B17), (B18) and (B31), one arrives at

$$\begin{aligned} \partial_t^{(1)} (\rho \mathbf{u} \otimes \mathbf{u} + p \mathbf{I}) = -\mathbf{u} \otimes [\nabla \cdot \rho \mathbf{u} \otimes \mathbf{u} + \nabla p] \\ - (\mathbf{u} \otimes [\nabla \cdot \rho \mathbf{u} \otimes \mathbf{u} + \nabla p])^\dagger + \mathbf{u} \otimes \mathbf{u} \nabla \cdot \rho \mathbf{u} \\ - (\nabla \cdot p \mathbf{u}) \mathbf{I} - \frac{R}{C_v} p (\nabla \cdot \mathbf{u}) \mathbf{I}. \end{aligned} \quad (\text{B46})$$

After applying the expansions

$$-\mathbf{u} \otimes \nabla \cdot \rho \mathbf{u} \otimes \mathbf{u} - (\mathbf{u} \otimes \nabla \cdot \rho \mathbf{u} \otimes \mathbf{u})^\dagger + \mathbf{u} \otimes \mathbf{u} \nabla \cdot \rho \mathbf{u} = -\nabla \cdot \rho \mathbf{u} \otimes \mathbf{u} \otimes \mathbf{u}, \quad (\text{B47})$$

$$-\mathbf{u} \otimes \nabla p = -(\nabla p \mathbf{u})^\dagger + p (\nabla \mathbf{u})^\dagger, \quad (\text{B48})$$

$$-(\mathbf{u} \otimes \nabla p)^\dagger = -\nabla p \mathbf{u} + p \nabla \mathbf{u}, \quad (\text{B49})$$

and plugging into Eq. (B44), most terms cancel and one obtains

$$\int \mathbf{v} \otimes \mathbf{v} f^{(1)} d\mathbf{v} = -\{\tau_1, \tau_2\} p \left[\nabla \mathbf{u} + \nabla \mathbf{u}^\dagger - \frac{R}{C_v} (\nabla \cdot \mathbf{u}) \mathbf{I} \right]. \quad (\text{B50})$$

Plugging this final expression into the momentum balance equation at order ε^2 , i.e. Eq. (B42), results in

$$\partial_t^{(2)} (\rho \mathbf{u}) + \nabla \cdot \boldsymbol{\tau}_{\text{NS}} = 0, \quad (\text{B51})$$

where the deviatoric Cauchy stress tensor in the NSF equations, i.e. the Navier–Stokes stress tensor, is correctly recovered as

$$\begin{aligned} \boldsymbol{\tau}_{\text{NS}} = -\{\tau_1, \tau_2\} p \left[\nabla \mathbf{u} + \nabla \mathbf{u}^\dagger - \frac{R}{C_v} (\nabla \cdot \mathbf{u}) \mathbf{I} \right] \\ = -\{\tau_1, \tau_2\} p \left[\nabla \mathbf{u} + \nabla \mathbf{u}^\dagger - \frac{2}{D} (\nabla \cdot \mathbf{u}) \mathbf{I} \right] \\ - \{\tau_1, \tau_2\} p \left(\frac{2}{D} - \frac{R}{C_v} \right) (\nabla \cdot \mathbf{u}) \mathbf{I}, \end{aligned} \quad (\text{B52})$$

with the dynamic shear viscosity, second viscosity, and dynamic bulk viscosity given as

$$\mu = \{\tau_1, \tau_2\} p, \quad (\text{B53})$$

$$\lambda = -\{\tau_1, \tau_2\} p \frac{R}{C_v}, \quad (\text{B54})$$

$$\eta = \{\tau_1, \tau_2\} p \left(\frac{2}{D} - \frac{R}{C_v} \right). \quad (\text{B55})$$

Moving on to computing the moments $\{(I) \int g d\mathbf{v}, (II) \int g + \frac{v^2}{2} f d\mathbf{v}\}$ for the energy balance at order ε^2 ,

$$(I) \quad \partial_t^{(2)} E + \nabla \cdot \int \mathbf{v} g^{(1)} d\mathbf{v} = 0,$$

$$(II) \quad \partial_t^{(2)} E + \nabla \cdot \int \mathbf{v} g^{(1)} + \mathbf{v} \frac{v^2}{2} f^{(1)} d\mathbf{v} = 0, \quad (\text{B56})$$

are obtained for the total energy split and the internal non-translational split, respectively. The flux terms can be further expanded using the moments $\{(I) \int \mathbf{v} g d\mathbf{v}, (II) \int \mathbf{v} g + \mathbf{v} \frac{v^2}{2} f d\mathbf{v}\}$ of the first-order-in- ε equation, rearranged as

$$\begin{aligned} (I) \quad -\frac{1}{\tau_1} \int \mathbf{v} g^{(1)} d\mathbf{v} + \left(\frac{1}{\tau_1} - \frac{1}{\tau_2} \right) \int \mathbf{v} g^{*(1)} d\mathbf{v} \\ = \partial_t^{(1)} \int \mathbf{v} g^{(0)} d\mathbf{v} + \nabla \cdot \int \mathbf{v} \otimes \mathbf{v} g^{(0)} d\mathbf{v}, \end{aligned}$$

$$\begin{aligned} (II) \quad -\frac{1}{\tau_1} \int \mathbf{v} g^{(1)} + \mathbf{v} \frac{v^2}{2} f^{(1)} d\mathbf{v} \\ + \left(\frac{1}{\tau_1} - \frac{1}{\tau_2} \right) \int \mathbf{v} g^{*(1)} + \mathbf{v} \frac{v^2}{2} f^{*(1)} d\mathbf{v} \\ = \partial_t^{(1)} \int \mathbf{v} g^{(0)} + \mathbf{v} \frac{v^2}{2} f^{(0)} d\mathbf{v} \\ + \nabla \cdot \int \mathbf{v} \otimes \mathbf{v} g^{(0)} + \mathbf{v} \otimes \mathbf{v} \frac{v^2}{2} f^{(0)} d\mathbf{v}, \end{aligned} \quad (\text{B57})$$

respectively. Plugging the equilibrium moments into the RHS results in

$$\left. \begin{aligned} \text{(I)} \quad & -\frac{1}{\tau_1} \int \mathbf{v} g^{(1)} d\mathbf{v} + \left(\frac{1}{\tau_1} - \frac{1}{\tau_2} \right) \int \mathbf{v} g^{*(1)} d\mathbf{v} \\ \text{(II)} \quad & -\frac{1}{\tau_1} \int \mathbf{v} g^{(1)} + \mathbf{v} \frac{v^2}{2} f^{(1)} d\mathbf{v} \\ & + \left(\frac{1}{\tau_1} - \frac{1}{\tau_2} \right) \int \mathbf{v} g^{*(1)} + \mathbf{v} \frac{v^2}{2} f^{*(1)} d\mathbf{v} \end{aligned} \right\} \\ & = \partial_t^{(1)} (p+E) \mathbf{u} + \nabla \cdot \left(\frac{p}{\rho} (E+p) \mathbf{I} \right. \\ & \left. + p \mathbf{u} \otimes \mathbf{u} + (p+E) \mathbf{u} \otimes \mathbf{u} \right), \quad (\text{B58})$$

which can be simplified by using the balance equation for $p\mathbf{u}$ and $E\mathbf{u}$, i.e. Eqs. (B36) and (B40), to replace the time derivatives in favor of space derivatives. Applying $E/\rho = C_v T + 1/2 u^2$ and $p/\rho = RT$ after the expansions

$$\nabla \left(\frac{pE}{\rho} \right) - \frac{E}{\rho} \nabla p = p \nabla \left(\frac{E}{\rho} \right) = p C_v \nabla T + p \nabla \left(\frac{u^2}{2} \right), \quad (\text{B59})$$

$$\nabla \left(\frac{p^2}{\rho} \right) - \frac{p}{\rho} \nabla p = p \nabla \left(\frac{p}{\rho} \right) = p R \nabla T, \quad (\text{B60})$$

together with the identity $\nabla \left(\frac{u^2}{2} \right) = \mathbf{u} \cdot (\nabla \mathbf{u})^\dagger$, leads to most terms canceling and one obtains

$$\left. \begin{aligned} \text{(I)} \quad & -\frac{1}{\tau_1} \int \mathbf{v} g^{(1)} d\mathbf{v} + \left(\frac{1}{\tau_1} - \frac{1}{\tau_2} \right) \int \mathbf{v} g^{*(1)} d\mathbf{v} \\ \text{(II)} \quad & -\frac{1}{\tau_1} \int \mathbf{v} g^{(1)} + \mathbf{v} \frac{v^2}{2} f^{(1)} d\mathbf{v} \\ & + \left(\frac{1}{\tau_1} - \frac{1}{\tau_2} \right) \int \mathbf{v} g^{*(1)} + \mathbf{v} \frac{v^2}{2} f^{*(1)} d\mathbf{v} \end{aligned} \right\} \\ & = p (C_v + R) \nabla T + p \left[\mathbf{u} \cdot \nabla \mathbf{u} + \mathbf{u} \cdot \nabla \mathbf{u}^\dagger \right. \\ & \left. - \frac{R}{C_v} \mathbf{u} (\nabla \cdot \mathbf{u}) \right] \quad (\text{B61})$$

Here again, the expansion depends on the construction of the quasi-equilibria attractors depending on the case of $\{\text{Pr} \leq 1, \text{Pr} \geq 1\}$. After applying the solvability conditions for the QE terms on the LHS,

$$\left. \begin{aligned} \text{(I)} \quad & \int \mathbf{v} g^{(1)} d\mathbf{v} \\ \text{(II)} \quad & \int \mathbf{v} g^{(1)} + \mathbf{v} \frac{v^2}{2} f^{(1)} d\mathbf{v} \end{aligned} \right\} = -\{\tau_2, \tau_1\} p (C_v + R) \nabla T \\ - \{\tau_1, \tau_2\} p \left[\mathbf{u} \cdot \nabla \mathbf{u} + \mathbf{u} \cdot \nabla \mathbf{u}^\dagger - \frac{R}{C_v} \mathbf{u} (\nabla \cdot \mathbf{u}) \right] \quad (\text{B62})$$

are received. Note that the solvability conditions for $\text{Pr} < 1$, i.e. (B14), result in τ_2 as the prefactor in front of the first term and τ_1 in front of the second term on the RHS, respectively, and vice versa for the case of $\text{Pr} > 1$ with (B16). This result

leads to the balance equation for total energy at order ε^2 , i.e. after plugging into (B56), as

$$\partial_t^{(2)} E + \nabla \cdot \mathbf{q}_{\text{NSF}} = 0, \quad (\text{B63})$$

where in

$$\mathbf{q}_{\text{NSF}} = \mathbf{q}_F + \mathbf{q}_H, \quad (\text{B64})$$

the viscous heating vector

$$\mathbf{q}_H = \mathbf{u} \cdot \boldsymbol{\tau}_{\text{NS}}, \quad (\text{B65})$$

composed of the Navier–Stokes stress tensor, cf. (B52), can be identified. Also the Fourier heat flux can consistently be recovered as

$$\mathbf{q}_F = -\kappa \nabla T, \quad (\text{B66})$$

where the thermal conductivity is given by

$$\kappa = \{\tau_2, \tau_1\} p \underbrace{(C_v + R)}_{C_p}. \quad (\text{B67})$$

The Prandtl number is readily shown to be,

$$\text{Pr} = \frac{\nu}{\alpha} = \frac{C_p \mu}{\kappa} = \frac{C_p \{\tau_1, \tau_2\} p}{\{\tau_2, \tau_1\} (C_v + R) p} = \frac{\{\tau_1, \tau_2\}}{\{\tau_2, \tau_1\}}, \quad (\text{B68})$$

with $\text{Pr} = 1$ in the limit of a BGK collision operator, $\tau_1 = \tau_2$. Truncating at this level, i.e. ε times Eq. {(B17), (B18), (B19)} plus ε^2 times Eq. {(B41), (B51), (B63)} and using Eq. (B5) truncated at $\partial_t = \partial_t^{(1)} + \varepsilon \partial_t^{(2)} + \mathcal{O}(\varepsilon^2)$, results in the equations

$$\partial_t \rho + \nabla \cdot \rho \mathbf{u} = 0, \quad (\text{B69})$$

$$\partial_t (\rho \mathbf{u}) + \nabla \cdot (\rho \mathbf{u} \otimes \mathbf{u} + p \mathbf{I} + \varepsilon \boldsymbol{\tau}_{\text{NS}}) = 0, \quad (\text{B70})$$

$$\partial_t E + \nabla \cdot [(E+p) \mathbf{u} + \varepsilon \mathbf{q}_F + \varepsilon \mathbf{u} \cdot \boldsymbol{\tau}_{\text{NS}}] = 0, \quad (\text{B71})$$

after transforming back to dimensional variables. The dissipative mechanisms, i.e. the Navier–Stokes stress tensor, the Fourier heat flux and the viscous heating vector, are of order $\mathcal{O}(\varepsilon) \sim \mathcal{O}(\text{Kn})$.

This concludes the multiscale analysis recovering the NSF equations.

Appendix C: Background on Hermite polynomials and the Grad expansion

The Hermite polynomial of order n is defined as

$$\mathcal{H}_n(x) = \frac{(-1)^n}{w(x)} \partial_x^n w(x), \quad (\text{C1})$$

where the normalized weight function is defined as

$$w(x) = \frac{1}{\sqrt{2\pi}} e^{-\frac{x^2}{2}}. \quad (\text{C2})$$

Hermite polynomials are mutually orthogonal with respect to the weight function $w(x)$, as

$$\int_{-\infty}^{+\infty} \mathcal{H}_m(x)w(x)\mathcal{H}_n(x)dx = n!\delta_{mn}, \quad (\text{C3})$$

and form a complete orthonormal basis of Hilbert space functions $f(x)$ satisfying the weighted Lebesgue integral in $L_w^2(\mathbb{R})$, i.e.,

$$\int_{-\infty}^{+\infty} |f(x)|^2 w(x)dx < \infty. \quad (\text{C4})$$

Hence, any function $f(x)$ can be expanded in terms of Hermite polynomials as

$$f(x) = \sum_{n=0}^{\infty} a_n \mathcal{H}_n(x), \quad (\text{C5})$$

where a_n is the Hermite coefficient of order n . By multiplying both sides with $\mathcal{H}_m(x)w(x)$, integrating over x and using the mutual orthogonality relation, the Hermite coefficients are found as

$$a_m = \frac{1}{m!} \int_{-\infty}^{+\infty} \mathcal{H}_m(x)w(x)f(x)dx. \quad (\text{C6})$$

Moving on to the multivariate case in D dimensions, using \mathbf{r} as the coordinate, the Hermite polynomial tensor of order n is defined as

$$\mathcal{H}_n(\mathbf{r}) = \frac{(-1)^n}{w(\mathbf{r})} \nabla^n w(\mathbf{r}), \quad (\text{C7})$$

where \mathcal{H}_n and ∇^n are tensors of rank n and $w(\mathbf{r})$ is the normalized multivariate Gaussian weight function defined as

$$w(\mathbf{r}) = \frac{1}{(2\pi)^{D/2}} e^{-\frac{\mathbf{r}^2}{2}}. \quad (\text{C8})$$

The Hermite polynomial tensors are mutually orthogonal with respect to the weight function $w(\mathbf{r})$, as

$$\int_{\mathbb{R}^D} w(\mathbf{r}) \mathcal{H}_{\chi_1}(\mathbf{r}) : \mathcal{H}_{\chi_2}(\mathbf{r}) d\mathbf{r} = n! \delta_{\chi_1, \chi_2}, \quad (\text{C9})$$

where χ_1 and χ_2 denote the set of indices $\{\alpha, \beta, \gamma, \delta, \dots\}$, and the Kronecker delta $\delta_{\chi_1, \chi_2} = 1$ if the indices are permutations of each other. They form a complete orthonormal basis of Hilbert space functions $f(\mathbf{r})$ satisfying the weighted Lebesgue integral in $L_w^2(\mathbb{R}^D)$, i.e.,

$$\int_{-\infty}^{+\infty} |f(\mathbf{r})|^2 w(\mathbf{r}) d\mathbf{r} < \infty. \quad (\text{C10})$$

Hence, any function $f(\mathbf{r})$ can be expanded in terms of Hermite polynomials as

$$f(\mathbf{r}) = \sum_{n=0}^{\infty} a_n : \mathcal{H}_n(\mathbf{r}), \quad (\text{C11})$$

where a_n is the Hermite coefficient tensor of order n . By multiplying both sides with $\mathcal{H}_m(\mathbf{r})w(\mathbf{r})$, integrating over \mathbf{r} and

using the mutual orthogonality relation, the Hermite coefficients are found as

$$a_m = \frac{1}{m!} \int_{-\infty}^{+\infty} \mathcal{H}_m(\mathbf{r})w(\mathbf{r})f(\mathbf{r})d\mathbf{r}. \quad (\text{C12})$$

In principle, any orthonormal basis can be used to discretize the (Maxwell-Boltzmann) distribution function. Note that the normalized weight function is of Gaussian nature, which marks an inherent advantage for Hermite polynomials as the orthonormal basis, besides the relation between the Hermite coefficients \mathbf{a}_n and the macroscopic variables of interest. Choosing the abscissae, i.e. the discrete velocity set, to be the roots of the orthogonal polynomial of the corresponding degree n results in the maximum algebraic degree of precision of $2Q - 1$. Hence the set of Hermite polynomials also guarantees best convergence of the approximation. Harold Grad first introduced the Hermite based discretization of the distribution function in 1949 [52]. Moments of the distribution function can be computed and reformulated using the Hermite basis as

$$\mathbf{M}_n = \int_{\mathbb{R}^D} \overbrace{\mathbf{v} \otimes \dots \otimes \mathbf{v}}^n f d\mathbf{v} = \int_{\mathbb{R}^D} w(\mathbf{v}) P_{(\infty)} d\mathbf{v}, \quad (\text{C13})$$

where P_{∞} is the polynomial function of the variable \mathbf{v} with order ∞ , defined as

$$P_{\infty}(\mathbf{v}, \rho, \mathbf{u}, T) = \frac{\overbrace{\mathbf{v} \otimes \dots \otimes \mathbf{v}}^n f(\mathbf{v}, \rho, \mathbf{u}, T)}{w(\mathbf{v})}. \quad (\text{C14})$$

Since only a certain amount of moments are needed to correctly recover the the solution of the Boltzmann equation for a targeted regime, e.g. Navier–Stokes–Fourier equations, the polynomial function $P_{(\infty)}$ can be truncated. Note that higher-order polynomials have no effect on lower order terms as the Hermite basis marks weighted orthonormal functions. Hence, the finite-order polynomial function,

$$P_M(\mathbf{v}, \rho, \mathbf{u}, T) = \frac{\overbrace{\mathbf{v} \otimes \dots \otimes \mathbf{v}}^n f_N(\mathbf{v}, \rho, \mathbf{u}, T)}{w(\mathbf{v})}, \quad (\text{C15})$$

where $M = 2N$, and N corresponds to the highest-order moment involved in the targeted hydrodynamics, can be used to evaluate Eq. (C13) as

$$\mathbf{M}_n = \int_{\mathbb{R}^D} w(\mathbf{v}) P_M d\mathbf{v} = \sum_{i=0}^{Q-1} w_i P_M(\mathbf{v}_i, \rho, \mathbf{u}, T), \quad (\text{C16})$$

using the discrete sum via the Gauss–Hermite quadrature. Note that \mathbf{v}_i are the discrete abscissae used for the quadrature and w_i the corresponding weights computed as

$$w_i = n! \mathcal{H}_{n-1}(v_i)^{-2}, \quad (\text{C17})$$

which corresponds to the product of the w_i in each direction in the multivariate case. Hence, the Grad expansion truncated at order $n = N$ can be written as

$$f_{i,N} = \sum_{n=0}^N a_n : \mathcal{H}_n(\mathbf{v}_i). \quad (\text{C18})$$

Further, to correctly recover the highest order moment of the targeted hydrodynamics with maximum precision using the Gauss-Hermite quadrature, $M \leq 2Q - 1$ must be fulfilled.

Appendix D: Hermite polynomials and coefficients of the Grad expansion

In notation mostly adopted in the lattice Boltzmann community, the Grad expansion [52] of a discrete population reads

$$\{f_i, g_i\} = w_i \sum_{n=0}^N \frac{1}{n!(RT_{ref})^n} \mathbf{a}_n(\{f, g\}) : \mathcal{H}_n(\mathbf{v}_i), \quad (\text{D1})$$

where N is the order of the expansion. Further, R is the specific gas constant, w_i , \mathbf{v}_i , and T_{ref} are the weights, the discrete particle velocities and the reference temperature of the velocity set, and ":" denotes the Frobenius inner product, i.e. the inner product with full contraction between the Hermite coefficient tensors \mathbf{a}_n and the Hermite polynomial tensors \mathcal{H}_n . The \mathcal{H}_n are parametrized by the discrete velocities, whereas the \mathbf{a}_n take into account a set of moments up to order N , i.e. $\{M_{n=0}, \dots, M_{n=N}\}$ such that the populations f_i and g_i expanded up to order N correctly reproduce the same set of moments, where

$$\mathbf{M}_n(\{f, g\}) = \sum_{i=0}^{Q-1} \overbrace{v_i \otimes \dots \otimes v_i}^n \{f_i, g_i\}. \quad (\text{D2})$$

For the computation of equilibrium populations f_i^{eq} and g_i^{eq} , the coefficients \mathbf{a}_n^{eq} are found as a function of the set of equilibrium moments $\{M_{n=0}^{\text{eq}}, \dots, M_{n=N}^{\text{eq}}\}$.

In the following, the Hermite polynomial tensors \mathcal{H}_n are given up to $N = 4$ using index notation, followed by the coefficient tensors \mathbf{a}_n for the case with arbitrary moments and explicitly evaluated with equilibrium moments, respectively. The Hermite polynomial tensors are found as

$$\mathcal{H}_0 = 1, \quad (\text{D3})$$

$$\mathcal{H}_\alpha = v_{i\alpha}, \quad (\text{D4})$$

$$\mathcal{H}_{\alpha\beta} = v_{i\alpha}v_{i\beta} - RT_{ref}\delta_{\alpha\beta}, \quad (\text{D5})$$

$$\mathcal{H}_{\alpha\beta\gamma} = v_{i\alpha}v_{i\beta}v_{i\gamma} - RT_{ref}[v_{i\alpha}\delta_{\beta\gamma}]_{\text{cyc}}, \quad (\text{D6})$$

$$\begin{aligned} \mathcal{H}_{\alpha\beta\gamma\delta} &= v_{i\alpha}v_{i\beta}v_{i\gamma}v_{i\delta} - RT_{ref}[v_{i\alpha}v_{i\beta}\delta_{\gamma\delta}]_{\text{cyc}} \\ &\quad + (RT_{ref})^2[\delta_{\alpha\beta}\delta_{\gamma\delta}]_{\text{cyc}}, \end{aligned} \quad (\text{D7})$$

and the contracted Hermite polynomial tensors of order three and four as

$$\mathcal{H}_{\alpha\beta\beta} = v_{i\alpha}(v_i^2 - RT_{ref}(D+2)), \quad (\text{D8})$$

$$\begin{aligned} \mathcal{H}_{\alpha\beta\gamma\gamma} &= v_{i\alpha}v_{i\beta}(v_i^2 - RT_{ref}(D+4)) \\ &\quad - RT_{ref}\delta_{\alpha\beta}(v_i^2 - RT_{ref}(D+2)), \end{aligned} \quad (\text{D9})$$

where "[]_{cyc}" denotes cyclic non-repetitive permutation over the indices and D is the physical dimension. Depending on the model, the contracted tensors can be sufficient compared

to the full tensors at the same expansion order. The corresponding Hermite coefficient tensors for arbitrary moments, here denoted in semi-recursive form, are found as

$$a_0 = M_0, \quad (\text{D10})$$

$$a_\alpha = M_\alpha, \quad (\text{D11})$$

$$a_{\alpha\beta} = M_{\alpha\beta} - RT_{ref}a_0\delta_{\alpha\beta}, \quad (\text{D12})$$

$$a_{\alpha\beta\gamma} = M_{\alpha\beta\gamma} - RT_{ref}[a_\alpha\delta_{\beta\gamma}]_{\text{cyc}}, \quad (\text{D13})$$

$$\begin{aligned} a_{\alpha\beta\gamma\delta} &= M_{\alpha\beta\gamma\delta} - RT_{ref}[a_{\alpha\beta}\delta_{\gamma\delta}]_{\text{cyc}} \\ &\quad - (RT_{ref})^2a_0[\delta_{\alpha\beta}\delta_{\gamma\delta}]_{\text{cyc}}, \end{aligned} \quad (\text{D14})$$

and the contracted tensors of order three and four as

$$a_{\alpha\beta\beta} = M_{\alpha\beta\beta} - RT_{ref}a_\alpha(D+2), \quad (\text{D15})$$

$$\begin{aligned} a_{\alpha\beta\gamma\gamma} &= M_{\alpha\beta\gamma\gamma} - RT_{ref}(a_{\alpha\beta}(D+4) + a_{\gamma\gamma}\delta_{\alpha\beta}) \\ &\quad - (RT_{ref})^2a_0\delta_{\alpha\beta}(D+2). \end{aligned} \quad (\text{D16})$$

At equilibrium, the Hermite coefficient tensors written out explicitly read

$$a_0^{\text{eq}} = \rho, \quad (\text{D17})$$

$$a_\alpha^{\text{eq}} = \rho u_\alpha, \quad (\text{D18})$$

$$a_{\alpha\beta}^{\text{eq}} = \rho u_\alpha u_\beta + RT_{ref}(\theta - 1)\rho\delta_{\alpha\beta}, \quad (\text{D19})$$

$$a_{\alpha\beta\gamma}^{\text{eq}} = \rho u_\alpha u_\beta u_\gamma + RT_{ref}(\theta - 1)[\rho u_\alpha\delta_{\beta\gamma}]_{\text{cyc}}, \quad (\text{D20})$$

$$\begin{aligned} a_{\alpha\beta\gamma\delta}^{\text{eq}} &= \rho u_\alpha u_\beta u_\gamma u_\delta + RT_{ref}(\theta - 1)[\rho u_\alpha u_\beta\delta_{\gamma\delta}]_{\text{cyc}} \\ &\quad + (RT_{ref})^2(\theta - 1)^2[\rho\delta_{\alpha\beta}\delta_{\gamma\delta}]_{\text{cyc}}, \end{aligned} \quad (\text{D21})$$

$$a_{\alpha\beta\beta}^{\text{eq}} = \rho u_\alpha (u^2 + RT_{ref}(\theta - 1)(D+2)), \quad (\text{D22})$$

$$\begin{aligned} a_{\alpha\beta\gamma\gamma}^{\text{eq}} &= \rho u_\alpha u_\beta (u^2 + RT_{ref}(\theta - 1)(D+4)) \\ &\quad + RT_{ref}(\theta - 1)\delta_{\alpha\beta}(u^2 + RT_{ref}(\theta - 1)(D+2)), \end{aligned} \quad (\text{D23})$$

where the normalized temperature is defined as $\theta = T/T_{ref}$.

Appendix E: Requirements on the phase-space discretization

In order to capture the fundamental flow physical properties of the NSF equations in the hydrodynamic limit, all moments appearing in the phase-space continuous multiscale expansion have to be matched when computed with discrete quadratures.

In case of the total energy split, this means that the f -distribution needs to properly recover the continuity and momentum balance equations to the Navier–Stokes order in the Chapman–Enskog expansion, including the dissipative fluxes, i.e. the non-equilibrium moments, appearing in the Navier–Stokes stress tensor $\boldsymbol{\tau}_{\text{NS}}$, which involve equilibrium moments up to order three of the f -distribution. Hence,

$$(I) \quad \int \mathbf{v} \otimes \mathbf{v} \otimes \mathbf{v} f^{\text{eq}} d\mathbf{v} = \sum_{i=0}^{Q-1} \mathbf{v}_i \otimes \mathbf{v}_i \otimes \mathbf{v}_i f_i^{\text{eq}}, \quad (\text{E1})$$

and all equilibrium moments of lower order have to be satisfied, which requires at least an order three ($N = 3$) expansion

of the f -equilibria. The same consideration for the energy balance equation leads to the requirement that the dissipative fluxes have to be correctly recovered to the NSF level, hence

$$(I) \quad \int \mathbf{v} \otimes \mathbf{v} g^{\text{eq}} d\mathbf{v} = \sum_{i=0}^{Q-1} \mathbf{v}_i \otimes \mathbf{v}_i g_i^{\text{eq}}, \quad (\text{E2})$$

leading to a minimal expansion of order two ($N = 2$) of the g -equilibria. If the same velocity set is applied to both distributions, as the requirements on f are higher, this means that the requirements on g are automatically satisfied in case the requirements on f satisfied. For the quadrature order, this means that a third-order Grad expansion (that of the f -equilibria) needs to be accommodated, which requires a fourth-order quadrature (e.g. $DDQ4^D$ lattice) or a third-order quadrature (e.g. $DDQ3^D$ lattice) with correction terms [31, 50] for the incorrect third-order moments of f .

In case of the internal non-translational energy split, as some part of the f -distribution contributes to the balance equation for total energy, the requirements for recovering the NSF equations are up to the moment

$$(II) \quad \int \mathbf{v} \otimes \mathbf{v} g^{(0)} + \mathbf{v} \otimes \mathbf{v} \frac{v^2}{2} f^{(0)} d\mathbf{v}, \quad (\text{E3})$$

which means that the requirement for the g distribution,

$$(II) \quad \int \mathbf{v} \otimes \mathbf{v} g^{\text{eq}} d\mathbf{v} = \sum_{i=0}^{Q-1} \mathbf{v}_i \otimes \mathbf{v}_i g_i^{\text{eq}}, \quad (\text{E4})$$

i.e. a second-order ($N = 2$) expansion of the g -equilibria, still holds, however, the fourth-order equilibrium moment of f also has to be correctly recovered as

$$(II) \quad \int \mathbf{v} \otimes \mathbf{v} \otimes \mathbf{v} \otimes \mathbf{v} f^{\text{eq}} d\mathbf{v} = \sum_{i=0}^{Q-1} \mathbf{v}_i \otimes \mathbf{v}_i \otimes \mathbf{v}_i \otimes \mathbf{v}_i f_i^{\text{eq}}, \quad (\text{E5})$$

or at least the contracted fourth-order equilibrium moment of f , as

$$(II) \quad \int \mathbf{v} \otimes \mathbf{v} v^2 f^{\text{eq}} d\mathbf{v} = \sum_{i=0}^{Q-1} \mathbf{v}_i \otimes \mathbf{v}_i v_i^2 f_i^{\text{eq}}. \quad (\text{E6})$$

This can be achieved with a fourth-order Grad expansion ($N = 4$) for the f -equilibria and accommodated either through a fifth-order quadrature (e.g. $DDQ5^D$ lattice), a fourth-order quadrature (e.g. $DDQ4^D$ lattice) with correction terms for the incorrect (contracted) fourth-order moment of f , or a third-order quadrature (e.g. $DDQ3^D$ lattice) with correction terms for the incorrect third-order and (contracted) fourth-order moments of f .

Note that, to obtain the compressible Euler equations, the dissipative fluxes, i.e. the non-equilibrium pressure and energy flux tensors, don't have to be matched, hence only moments of up to one order less than for the NSF equations have to be correctly recovered. This also results in requirements to the order of the Grad expansion and the quadrature of one order less as compared to NSF.

Appendix F: Direct parametrization of the second distribution

The discrete g -equilibria can also be directly parametrized by the discrete f -equilibria as in the phase-space continuous kinetic model, cf. Eq. (36). This reads

$$(I) \quad g_i^{\text{eq}} = \left(C_v T - \frac{RDT}{2} + \frac{v_i^2}{2} \right) f_i^{\text{eq}}, \quad (\text{F1})$$

$$(II) \quad g_i^{\text{eq}} = \left(C_v T - \frac{RDT}{2} \right) f_i^{\text{eq}}. \quad (\text{F2})$$

While this parametrization simplifies the computation of the g_i^{eq} for the internal non-translational split, for the total energy split in increases the requirements on the phase-space discretization. This is due to the v_i^2 sitting in the link, increasing the requirements to a fourth-order ($N = 4$) expansion of the g_i -equilibria and therefore a fifth-order quadrature ($Q = 5^D$), i.e. the D2Q25 velocity set in $D = 2$. Note that an additional requirement for direct parametrization is the application of the same quadrature order, i.e. discrete velocity set, for both distributions, whereas this is not a necessity in case the g_i are constructed independently of the f_i using Grad-Hermite expansions.

Appendix G: Specifications of the velocity sets

The specifications, i.e. particle velocities, weights and reference temperatures, for the $DDQ4^D$ and $DDQ5^D$ velocity sets for $D = 2$ built with the Gauss-Hermite quadrature are listed in Table II and III, respectively.

D2Q16 (Hermite) for $T_{ref} = 1$		
i	$\mathbf{v}_i = (v_{ix}, v_{iy})$	w_i
0-3	$(\pm\sqrt{3}-\sqrt{6}, \pm\sqrt{3}-\sqrt{6})$	$\frac{3+\sqrt{6}}{12} \frac{3+\sqrt{6}}{12}$
4-7	$(\pm\sqrt{3}-\sqrt{6}, \pm\sqrt{3}+\sqrt{6})$	$\frac{3+\sqrt{6}}{12} \frac{3-\sqrt{6}}{12}$
8-11	$(\pm\sqrt{3}+\sqrt{6}, \pm\sqrt{3}-\sqrt{6})$	$\frac{3-\sqrt{6}}{12} \frac{3+\sqrt{6}}{12}$
12-15	$(\pm\sqrt{3}+\sqrt{6}, \pm\sqrt{3}+\sqrt{6})$	$\frac{3-\sqrt{6}}{12} \frac{3-\sqrt{6}}{12}$

TABLE II. Fourth-order quadrature in two dimensions (D2Q16).

D2Q25 (Hermite) for $T_{ref} = 1$		
i	$\mathbf{v}_i = (v_{ix}, v_{iy})$	w_i
0	(0, 0)	$\frac{8}{15}$
1, 3	$(\pm\sqrt{5}-\sqrt{10}, 0)$	$\frac{8}{15} (7+2\sqrt{10})$
2, 4	$(0, \pm\sqrt{5}-\sqrt{10})$	$(7+2\sqrt{10}) \frac{8}{15}$
5, 6, 7, 8	$(\pm\sqrt{5}-\sqrt{10}, \pm\sqrt{5}-\sqrt{10})$	$(7+2\sqrt{10}) (7+2\sqrt{10})$
9, 11	$(\pm\sqrt{5}+\sqrt{10}, 0)$	$(7-2\sqrt{10}) \frac{8}{15}$
10, 12	$(0, \pm\sqrt{5}+\sqrt{10})$	$\frac{8}{15} (7-2\sqrt{10})$
13, 16, 17, 20	$(\pm\sqrt{5}+\sqrt{10}, \pm\sqrt{5}-\sqrt{10})$	$(7-2\sqrt{10}) (7+2\sqrt{10})$
14, 15, 18, 19	$(\pm\sqrt{5}-\sqrt{10}, \pm\sqrt{5}+\sqrt{10})$	$(7+2\sqrt{10}) (7-2\sqrt{10})$
21, 22, 23, 24	$(\pm\sqrt{5}+\sqrt{10}, \pm\sqrt{5}+\sqrt{10})$	$(7-2\sqrt{10}) (7-2\sqrt{10})$

TABLE III. Fifth-order quadrature in two dimensions (D2Q25).

REFERENCES

- [1] Sergio Pirozzoli. Numerical methods for high-speed flows. *Annual review of fluid mechanics*, 43(1):163–194, 2011.
- [2] H. C. Yee and Björn Sjögren. Recent developments in accuracy and stability improvement of nonlinear filter methods for dns and les of compressible flows. *computers & Fluids*, 169:331–348, 2018.
- [3] Timm Krüger, Halim Kusumaatmaja, Alexandr Kuzmin, Orest Shardt, Goncalo Silva, and Erlend Magnus Viggen. The lattice Boltzmann method. *Springer International Publishing*, 10(978-3):4–15, 2017.
- [4] Sauro Succi. *The lattice Boltzmann equation: for fluid dynamics and beyond*. Oxford university press, 2001.
- [5] Ludwig Boltzmann. *Weitere studien über das wärme-gleichgewicht unter gasmolekülen*, volume 66. Aus der kk Hot-und Staatsdruckerei, 1872.
- [6] S. A. Hosseini and I. V. Karlin. Lattice Boltzmann for non-ideal fluids: Fundamentals and practice. *Physics Reports*, 1030:1–137, 2023.
- [7] Sydeny Chapman and T. G. Cowling. *The mathematical theory of non-uniform gases. an account of the kinetic theory of viscosity, thermal conduction and diffusion in gases*. 1970.
- [8] Prabhu Lal Bhatnagar, Eugene P. Gross, and Max Krook. A model for collision processes in gases. I. small amplitude processes in charged and neutral one-component systems. *Physical review*, 94(3):511, 1954.
- [9] Y. H. Qian, D. D’Humières, and P. Lallemand. Lattice bgk models for Navier-Stokes equation. *Europhysics Letters*, 17(6):479, 1992. URL <https://dx.doi.org/10.1209/0295-5075/17/6/001>.
- [10] Hudong Chen, Shiyi Chen, and William H. Matthaeus. Recovery of the Navier-Stokes equations using a lattice-gas Boltzmann method. *Phys. Rev. A*, 45:R5339–R5342, 1992. URL <https://link.aps.org/doi/10.1103/PhysRevA.45.R5339>.
- [11] Zhaoli Guo and Kun Xu. Progress of discrete unified gas-kinetic scheme for multiscale flows. *Advances in Aerodynamics*, 3:1–42, 2021.
- [12] Aiguo Xu, Guangcai Zhang, and Yudong Zhang. Discrete Boltzmann modeling of compressible flows. *Kinetic theory*, pages 450–458, 2018.
- [13] Luc Mieussens. Discrete-velocity models and numerical schemes for the Boltzmann-bgk equation in plane and axisymmetric geometries. *Journal of Computational Physics*, 162(2):429–466, 2000.
- [14] Seyed Ali Hosseini, Pierre Boivin, Dominique Thévenin, and Ilya Karlin. Lattice Boltzmann methods for combustion applications. *Progress in Energy and Combustion Science*, 102:101140, 2024.
- [15] Dominique D’Humières, Irina Ginzburg, Manfred Krafczyk, Pierre Lallemand, and Li-Shi Luo. Multiple-relaxation-time lattice Boltzmann models in three dimensions. *Philosophical Transactions of the Royal Society of London. Series A: Mathematical, Physical and Engineering Sciences*, 360(1792):437–451, 2002. URL <https://royalsocietypublishing.org/doi/abs/10.1098/rsta.2001.0955>.
- [16] Martin Geier, Andreas Greiner, and Jan G. Korvink. Cascaded digital lattice Boltzmann automata for high reynolds number flow. *Phys. Rev. E*, 73:066705, 2006. URL <https://link.aps.org/doi/10.1103/PhysRevE.73.066705>.
- [17] Martin Geier, Martin Schönherr, Andrea Pasquali, and Manfred Krafczyk. The cumulant lattice Boltzmann equation in three dimensions: Theory and validation. *computers & Mathematics with Applications*, 70(4):507–547, 2015. URL <https://www.sciencedirect.com/science/article/pii/S0898122115002126>.
- [18] Orestis Malaspinas. Increasing stability and accuracy of the lattice Boltzmann scheme: recursivity and regularization, 2015. URL <https://arxiv.org/abs/1505.06900>.
- [19] Ilya V. Karlin and S. Succi. Equilibria for discrete kinetic equations. *Phys. Rev. E*, 58:R4053–R4056, 1998. URL <https://link.aps.org/doi/10.1103/PhysRevE.58.R4053>.
- [20] I. V. Karlin, F. Bösch, and S. S. Chikatamarla. Gibbs’ principle for the lattice-kinetic theory of fluid dynamics. *Phys. Rev. E*, 90:031302, 2014. URL <https://link.aps.org/doi/10.1103/PhysRevE.90.031302>.
- [21] S. A. Hosseini, M. Atif, S. Ansumali, and I. V. Karlin. Entropic lattice Boltzmann methods: A review. *computers & Fluids*, 259:105884, 2023. URL <https://www.sciencedirect.com/science/article/pii/S0045793023001093>.
- [22] E. M. Shakhov. Generalization of the krook kinetic relaxation equation. *Fluid Dynamics*, 3(5):95–96, 1968. URL <https://doi.org/10.1007/BF01029546>.
- [23] Jr. Holway Lowell H. New statistical models for kinetic theory: Methods of construction. *The Physics of Fluids*, 9(9):1658–1673, 1966. URL <https://doi.org/10.1063/1.1761920>.
- [24] Alexander N. Gorban and Ilya V. Karlin. General approach to constructing models of the Boltzmann equation. *Physica A: Statistical Mechanics and its Applications*, 206:401–420, 1994.
- [25] Aleksandr Nikolaevich Gorban and Ilya V Karlin. *Invariant manifolds for physical and chemical kinetics*, volume 660. Springer, 2005.
- [26] S. Ansumali, S. Arcidiacono, S. S. Chikatamarla, N. I. Prasianakis, A. N. Gorban, and I. V. Karlin. Quasi-equilibrium lattice Boltzmann method. *The European Physical Journal B*, 56(2):135–139, 2007. URL <https://doi.org/10.1140/epjb/e2007-00100-1>.
- [27] Xiaoyi He, Shiyi Chen, and Gary D. Doolen. A novel thermal model for the lattice Boltzmann method in incompressible limit. *Journal of Computational Physics*, 146(1):282–300, 1998. ISSN 0021-9991. doi:<https://doi.org/10.1006/jcph.1998.6057>. URL <https://www.sciencedirect.com/science/article/pii/S0021999198960570>.
- [28] V. A. Rykov. A model kinetic equation for a gas with rotational degrees of freedom. *Fluid Dynamics*, 10(6):959–966, 1976.
- [29] I. V. Karlin, D. Sichau, and S. S. Chikatamarla. Consistent two-population lattice Boltzmann model for thermal flows. *Phys. Rev. E*, 88:063310, 2013. URL <https://link.aps.org/doi/10.1103/PhysRevE.88.063310>.
- [30] S. A. Hosseini, A. Bhadauria, and I. V. Karlin. Probing double-distribution-function models in discrete-velocity Boltzmann methods for highly compressible flows: Particles-on-demand realization. *Phys. Rev. E*, 110:045313, 2024. URL <https://link.aps.org/doi/10.1103/PhysRevE.110.045313>.
- [31] Nikolaos I. Prasianakis and Ilya V. Karlin. Lattice Boltzmann method for thermal flow simulation on standard lattices. *Phys. Rev. E*, 76:016702, 2007. URL <https://link.aps.org/doi/10.1103/PhysRevE.76.016702>.
- [32] Mohammad Hossein Saadat, Fabian Bösch, and Ilya V. Karlin. Lattice Boltzmann model for compressible flows on standard lattices: Variable prandtl number and adiabatic exponent. *Phys. Rev. E*, 99:013306, 2019. URL <https://link.aps.org/doi/10.1103/PhysRevE.99.013306>.

- [33] Seyed Ali Hosseini, Nasser Darabiha, and Dominique Thévenin. Compressibility in lattice Boltzmann on standard stencils: effects of deviation from reference temperature. *Philosophical Transactions of the Royal Society A*, 378(2175): 20190399, 2020.
- [34] Yongliang Feng, Pierre Sagaut, and Wenquan Tao. A three dimensional lattice model for thermal compressible flow on standard lattices. *Journal of Computational Physics*, 303:514–529, 2015. URL <https://www.sciencedirect.com/science/article/pii/S0021999115005926>.
- [35] Q. Li, K. H. Luo, Y. L. He, Y. J. Gao, and W. Q. Tao. Coupling lattice Boltzmann model for simulation of thermal flows on standard lattices. *Physical Review E—Statistical, Nonlinear, and Soft Matter Physics*, 85(1):016710, 2012.
- [36] Yongliang Feng, Pierre Sagaut, and Wen-Quan Tao. A compressible lattice Boltzmann finite volume model for high subsonic and transonic flows on regular lattices. *computers & Fluids*, 131:45–55, 2016. URL <https://www.sciencedirect.com/science/article/pii/S0045793016300652>.
- [37] Shyam S. Chikatamarla and Ilya V. Karlin. Entropy and galilean invariance of lattice Boltzmann theories. *Phys. Rev. Lett.*, 97:190601, 2006. URL <https://link.aps.org/doi/10.1103/PhysRevLett.97.190601>.
- [38] Nicolò Frapolli, S. Chikatamarla, and Ilya Karlin. Multispeed entropic lattice Boltzmann model for thermal flows. *Physical review. E, Statistical physics, plasmas, fluids, and related interdisciplinary topics*, 90, 2014.
- [39] Ruben M. Strässle, S. A. Hosseini, and I. V. Karlin. A fully conservative discrete velocity boltzmann solver with parallel adaptive mesh refinement for compressible flows. *Physics of Fluids*, 37(4):046110, 04 2025. ISSN 1070-6631. doi: 10.1063/5.0263958. URL <https://doi.org/10.1063/5.0263958>.
- [40] N. Frapolli, S. S. Chikatamarla, and I. V. Karlin. Lattice kinetic theory in a comoving galilean reference frame. *Phys. Rev. Lett.*, 117:010604, 2016. URL <https://link.aps.org/doi/10.1103/PhysRevLett.117.010604>.
- [41] S. A. Hosseini, C. Coreixas, N. Darabiha, and D. Thévenin. Extensive analysis of the lattice Boltzmann method on shifted stencils. *Phys. Rev. E*, 100:063301, 2019. URL <https://link.aps.org/doi/10.1103/PhysRevE.100.063301>.
- [42] Christophe Coreixas and Jonas Latt. Compressible lattice Boltzmann methods with adaptive velocity stencils: An interpolation-free formulation. *Physics of Fluids*, 32(11), 2020. URL <http://dx.doi.org/10.1063/5.0027986>.
- [43] B. Dorschner, F. Bösch, and I. V. Karlin. Particles on demand for kinetic theory. *Phys. Rev. Lett.*, 121: 130602, 2018. URL <https://link.aps.org/doi/10.1103/PhysRevLett.121.130602>.
- [44] N. Sawant, B. Dorschner, and I. V. Karlin. Detonation modeling with the particles on demand method. *AIP advances*, 12(7): 075107, 2022.
- [45] N. G. Kallikounis, B. Dorschner, and I. V. Karlin. Particles on demand for flows with strong discontinuities. *Phys. Rev. E*, 106:015301, Jul 2022. doi: 10.1103/PhysRevE.106.015301. URL <https://link.aps.org/doi/10.1103/PhysRevE.106.015301>.
- [46] N. G. Kallikounis and I. V. Karlin. Particles on demand method: Theoretical analysis, simplification techniques, and model extensions. *Phys. Rev. E*, 109:015304, 2024. URL <https://link.aps.org/doi/10.1103/PhysRevE.109.015304>.
- [47] Abhimanyu Bhadauria and Ilya Karlin. High speed flows with particles on demand: Boundary conditions. *computers & Fluids*, 271:106152, 2024. URL <https://www.sciencedirect.com/science/article/pii/S0045793023003778>.
- [48] Y. Ji, S. A. Hosseini, B. Dorschner, K. H. Luo, and I. V. Karlin. Eulerian discrete kinetic framework in comoving reference frame for hypersonic flows. *Journal of Fluid Mechanics*, 983: A11, 2024. URL <https://doi.org/10.1017/jfm.2024.94>.
- [49] N. Frapolli, S.S. Chikatamarla, and I.V. Karlin. Entropic lattice Boltzmann simulation of thermal convective turbulence. *Computers & Fluids*, 175:2–19, 2018. ISSN 0045-7930. doi:<https://doi.org/10.1016/j.compfluid.2018.08.021>. URL <https://www.sciencedirect.com/science/article/pii/S0045793018305218>.
- [50] Mohammad H. Saadat, Seyed A. Hosseini, Benedikt Dorschner, and I. V. Karlin. Extended lattice Boltzmann model for gas dynamics. *Physics of Fluids*, 33(4):046104, 2021.
- [51] C. David Levermore. Moment closure hierarchies for kinetic theories. *Journal of Statistical Physics*, 83(5):1021–1065, 1996. ISSN 1572-9613. doi:10.1007/BF02179552. URL <https://doi.org/10.1007/BF02179552>.
- [52] H. Grad. On the kinetic theory of rarefied gases. *Communications on pure and applied mathematics*, 2(4):331–407, 1949.
- [53] AN Gorban and IV Karlin. Quasi-equilibrium approximation and non-standard expansions in the theory of the Boltzmann kinetic equation. *Mathematical Modelling in Biology and Chemistry. New Approaches*, ed. RG Khlebopros, Nauka, Novosibirsk, pages 69–117, 1991.
- [54] Alexander N. Gorban and Iliya V. Karlin. Quasi-equilibrium closure hierarchies for the Boltzmann equation. *Physica A: Statistical Mechanics and its Applications*, 360(2):325–364, 2006. ISSN 0378-4371. doi:<https://doi.org/10.1016/j.physa.2005.07.016>. URL <https://www.sciencedirect.com/science/article/pii/S0378437105007557>.
- [55] N. Frapolli, S. S. Chikatamarla, and I. V. Karlin. Entropic lattice Boltzmann model for gas dynamics: Theory, boundary conditions, and implementation. *Physical Review E*, 93(6):063302, 2016.
- [56] André Bardow, Ilya V. Karlin, and Andrei A. Gusev. Multi-speed models in off-lattice Boltzmann simulations. *Phys. Rev. E*, 77:025701, 2008. URL <https://link.aps.org/doi/10.1103/PhysRevE.77.025701>.
- [57] N. G. Kallikounis, B. Dorschner, and I. V. Karlin. Multi-scale semi-lagrangian lattice Boltzmann method. *Phys. Rev. E*, 103:063305, 2021. URL <https://link.aps.org/doi/10.1103/PhysRevE.103.063305>.
- [58] Dominik Wilde, Andreas Krämer, Dirk Reith, and Holger Foysi. Semi-lagrangian lattice Boltzmann method for compressible flows. *Phys. Rev. E*, 101:053306, 2020. URL <https://link.aps.org/doi/10.1103/PhysRevE.101.053306>.
- [59] Dominik Wilde, Andreas Krämer, Mario Bedrunka, Dirk Reith, and Holger Foysi. Cubature rules for weakly and fully compressible off-lattice Boltzmann methods. *Journal of Computational Science*, 51:101355, 2021. URL <https://www.sciencedirect.com/science/article/pii/S1877750321000508>.
- [60] HX Zhang. Non-oscillatory and non-free-parameter dissipation difference scheme. *Acta Aerodynamica Sinica*, 6:143–165, 1988.
- [61] Hanxin Zhang and Fenggan Zhuang. Nnd schemes and their applications to numerical simulation of two- and three-dimensional flows. *Journal of Computational Physics*, 415: 109491, 2020.
- [62] Ami Harten and Stanley Osher. Uniformly high-order accurate nonoscillatory schemes. i. *SIAM Journal on Numerical*

- Analysis*, 24(2):279–309, 1987. doi:10.1137/0724022. URL <https://doi.org/10.1137/0724022>.
- [63] Bram van Leer. Towards the ultimate conservative difference scheme. *Journal of Computational Physics*, 135(2):229–248, 1997. ISSN 0021-9991. doi:<https://doi.org/10.1006/jcph.1997.5704>. URL <https://www.sciencedirect.com/science/article/pii/S0021999197957041>.
- [64] P. L. Roe. Characteristic-based schemes for the euler equations. *Annual Review of Fluid Mechanics*, 18:337–365, 1986. URL <https://www.annualreviews.org/doi/10.1146/annurev.fl.18.010186.002005>.
- [65] G. A. Sod. Review. a survey of several finite difference methods for systems of nonlinear hyperbolic conservation laws. *Journal of Computational Physics*, 27(1):1–31, 1978.
- [66] Paul J. Dellar. Bulk and shear viscosities in lattice Boltzmann equations. *Physical Review E*, 64(3):031203, 2001.
- [67] Osamu Inoue and Yuji Hattori. Sound generation by shock–vortex interactions. *Journal of Fluid Mechanics*, 380:81–116, 1999.
- [68] A. Tiwari and S. P. Vanka. A ghost fluid lattice boltzmann method for complex geometries. *International Journal for Numerical Methods in Fluids*, 69(2):481–498, 2012. doi:<https://doi.org/10.1002/flid.2573>. URL <https://onlinelibrary.wiley.com/doi/abs/10.1002/flid.2573>.
- [69] Zhaoli Guo, Chuguang Zheng, and Baochang Shi. An extrapolation method for boundary conditions in lattice boltzmann method. *Physics of Fluids*, 14(6):2007–2010, 06 2002. ISSN 1070-6631. doi:10.1063/1.1471914. URL <https://doi.org/10.1063/1.1471914>.
- [70] Anatol Roshko and Hans W. Liepmann. Elements of gas dynamics. 1957. URL <https://api.semanticscholar.org/CorpusID:198393709>.
- [71] Herbert S. Ribner. Cylindrical sound wave generated by shock-vortex interaction. *AIAA Journal*, 23(11):1708–1715, 1985. URL <https://doi.org/10.2514/3.9155>.
- [72] Janet L. Ellzey, Michael R. Henneke, J. Michael Picone, and Elaine S. Oran. The interaction of a shock with a vortex: Shock distortion and the production of acoustic waves. *Physics of Fluids*, 7(1):172–184, 1995. URL <https://doi.org/10.1063/1.868738>.
- [73] D. S. Dosanj and T. M. Weeks. Interaction of a starting vortex as well as a vortex street with a traveling shock wave. *AIAA Journal*, 3(2):216–223, 1965. URL <https://doi.org/10.2514/3.2833>.